Comprehensive Phase Behavior of Poly(isoprene-*b*-styrene-*b*-ethylene oxide) Triblock Copolymers

Joon Chatterjee, Sumeet Jain, and Frank S. Bates*

Department of Chemical Engineering and Materials Science, University of Minnesota, Minneapolis, Minnesota 55455

Received September 28, 2006; Revised Manuscript Received February 14, 2007

ABSTRACT: The phase behavior of 44 poly(isoprene-*b*-styrene-*b*-ethylene oxide) (ISO) linear triblock copolymer melts was investigated at weak to intermediate segregation strengths and spanning a comprehensive range of compositions. Phases were characterized by a combination of experimental techniques, including small-angle X-ray scattering, dynamic mechanical spectroscopy, transmission electron microscopy, and birefringence measurements. Combined with our previous results, six different stable ordered state symmetries have been identified: lamellae (LAM), *Fddd* orthorhombic network (O^{70}), double gyroid (Q^{230}), alternating gyroid (Q^{214}), hexagonal (HEX), and body-centered cubic (BCC). The phase map of ISO specimens was found to be somewhat asymmetric around the $f_I = f_O$ isopleth. This work provides a guide for theoretical studies and gives insight into the intricate effects of various parameters on the self-assembly of ABC triblock copolymers. Experimental SAXS data evaluated with a simple scattering intensity model show that local mixing varies continuously across the phase map between states of two- and three-domain segregation.

Introduction

More than four decades of research has established quantitative and predictive theoretical tools for anticipating the phase behavior of AB diblock copolymers, which complement a rich collection of experimental data.[1−7] Addition of a third chemically distinct C block to an AB diblock expands the phase complexity and the number of experimentally adjustable parameters, resulting in a fascinating, yet largely unpredictable, array of morphologies. Nearly three dozen ordered phases have been discovered in ABC triblocks[2,8−23] compared to just four well-established equilibrium phases in AB diblocks. This expanded scope is both stimulating and intimidating. Three different polymer blocks offers desirable features such as increased molecular design opportunities and increased functionality. However, additional blocks imply additional variables, with a geometrically expanding degree of complexity with each new element.

Self-assembly of block copolymers in the bulk liquid state is governed by three sets of parameters: composition, interfacial tension, and sequencing. (The block statistical segment lengths constitute a fourth, less critical, set of variables.) For AB diblocks there is one composition variable, $f_A = 1 - f_B$, one segment−segment interaction parameter, χ_{AB}, and one sequence. Linear ABC triblocks are governed by two independent composition variables, three χ_{ij}'s, and three distinct sequences. Choosing among these parameters in order to target a specific morphology for a particular application represents a daunting task, complicated by a lack of theoretical guidance and relatively few comprehensive experimental phase portraits.

Different types of ABC triblock copolymers (specifically referring to those in linear architectures and in the bulk liquid state) have been investigated by a host of research groups, such as Hashimoto et al.,[29,30] Matsushita et al.,[15,16,31,32] Stadler et al.,[9,10,14,33−36] Abetz et al.,[24−27] and Bates et al.[8,11−13,28] While this research has advanced our knowledge of self-assembly in ABC copolymers, new phases continue to be discovered; i.e., there is no universal conceptual organization at this time.

* Corresponding author. E-mail: bates@cems.umn.edu.

This publication is designed to provide a framework for better understanding ABC triblock copolymer phase behavior. Three common polymers, poly(isoprene) (I), poly(styrene) (S), and poly(ethylene oxide) (O), were polymerized into ISO triblock copolymers over a wide range of compositions and in proximity to the order−disorder transition temperature, i.e., at weak to intermediate segregation strength. Phase behavior was established using four techniques: small-angle X-ray scattering (SAXS), dynamic mechanical spectroscopy (DMS), transmission electron microscopy (TEM), and birefringence measurements. Six distinct ordered state symmetries were identified, each associated with a space-filling morphology: lamellae (LAM); hexagonal (HEX, assumed to be cylindrical); orthorhombic (*Fddd* space group, a network structure referred to as O^{70}); and three cubic states, BCC (assumed to be spherical), Q^{230} (space group $Ia\bar{3}d$, referred to as double gyroid), and Q^{214} (space group $I4_132$, known as alternating gyroid).

The present study is motivated by several previous publications from our research group that are related to the phase behavior of ISO triblocks. Bailey et al.[28] studied the phase map along a composition channel spanning a symmetric IS diblock and a symmetric ISO triblock. They first proposed the existence of the O^{70} phase in ISO and demonstrated the sequence of phase transformations LAM (2-domain) → O^{70} → LAM (3-domain) with increasing PEO content. Epps and Cochran et al.[12] explored the phase diagram further and confirmed the stability of the O^{70} phase and demonstrated the formation of three different network morphologies, Q^{230}, O^{70}, and Q^{214}, within a composition window bounded by $0.38 < f_S < 0.53$ and $0.13 < f_O < 0.25$. This publication builds on the above-mentioned reports and substantially expands the phase map over a comprehensive range of compositions. When combined with our previous results, a coherent picture emerges regarding the interplay between the molecular variables and phase selection. Of particular interest are the network phases (O^{70}, Q^{230}, Q^{214}), which we anticipate will have various exciting applications as membranes, filters, for drug delivery, and as other devices that mediate transport phenomena. This publication demonstrates that the O^{70} and Q^{230}

10.1021/ma062249s CCC: $37.00
Published on Web 03/22/2007

network phases exist in more than one location in the I−S−O three-parameter phase map. The combined results represent, to the best of our knowledge, the most comprehensive phase map for an ABC triblock copolymer. Along with a practical characterization of the ISO phase behavior, these findings offer a unique template against which self-consistent-field theory calculations can be compared.

Other publications from our group have described the effects of additional variables on the phase behavior of ABC systems. Epps et al.[37] studied the self-assembly of ISO triblocks at higher molecular weights and demonstrated that long-range order in the O^{70} morphology is disrupted as a consequence of restrained chain mobility. Cochran et al.[11] investigated poly(cyclohexylethylene-*b*-ethylethylene-*b*-ethylene) (CE_EE) and found that the O^{70} transformed into a lower symmetry O^{52} state during reciprocating shear deformation. In another study, Epps et al.[38] blended homopolymers of PI and PS with neat ISO triblocks thereby tuning the overall composition, demonstrating that modest amounts of homopolymer could induce phase transitions between neighboring ordered states.

Experimental Section

Synthesis. Poly(isoprene-*b*-styrene-*b*-ethylene oxide) (ISO) triblock copolymers were synthesized using a two-step anionic polymerization technique.[8,39] In the first step, poly(isoprene-*b*-styrene) diblock copolymer was prepared by initiation of *sec*-butyllithium and polymerization of isoprene followed by addition and reaction of styrene monomer to near completion. Termination with excess ethylene oxide and then methanol produces a terminal hydroxyl group on the diblock chains (IS-OH). In the second step, small batches of the diblock copolymer were reinitiated with potassium napthalenide, and ethylene oxide was added to form the third block. This synthetic procedure resulted in nearly monodisperse ISO triblock copolymers (polydispersity indices, PDIs < 1.2) with precise control over composition and molecular weight. Additional synthetic details can be found in the literature.[39]

Chemical Characterization. The compositions of the ISO triblocks were determined by ^{1}H NMR spectroscopy using a 300 MHz Varian instrument running at room temperature with deuterated chloroform as the solvent. The mole fractions of isoprene, styrene, and ethylene oxide repeat units estimated from the integrated NMR spectra were converted to monomer volume fractions f_I, f_S, and f_O on the basis of published homopolymer densities at 140 °C ($\rho_I = 0.830$, $\rho_S = 0.969$, $\rho_O = 1.064$ in g/cm^3).[40]

The overall number-average triblock molecular weight, $M_{n,ISO}$, was computed from the absolute number-average molecular weight, $M_{n,I}$, of the I block and the weight fraction w_I of the I block in the ISO triblock. w_I was calculated from the mole fraction of isoprene repeat units in the ISO triblock (determined from NMR spectra) and the density of poly(isoprene). For determining $M_{n,I}$, an aliquot of the reaction mixture was extracted after complete reaction of isoprene monomer and before the styrene monomer was added, and size exclusion chromatography (SEC) was performed with THF as carrier solvent; the SEC instrument was configured with a light scattering detector. A differential refractive index $dn/dc = 0.124$ cm^3/g was used for poly(isoprene) in THF to analyze the SEC data.

Polydispersities of all ISO triblock copolymers were also determined by SEC and were found to be expectedly low, PDI < 1.2. Table 1 lists the chemical characterization data for all the ISO specimens.

SAXS. Synchrotron source small-angle X-ray scattering (SAXS) experiments were conducted at the DuPont-Northwestern-Dow Synchrotron Research Center at the Advanced Photon Source using sample−detector distances of between 3 and 6.6 m and X-ray wavelengths of 1.54 and 0.73 Å. Data were acquired with a Mar CCD area detector and are referred to as 2D-SAXS patterns. Sample temperature was controlled to within ±1 °C using a DSC chamber maintained under a helium purge. All samples were conditioned prior to traveling to the synchrotron facility by annealing, typically at 160 °C under vacuum for 2 h, except for samples that displayed order−order transitions (OOT), which were annealed at 90−100 °C under vacuum for 2 h. At the synchrotron facility, samples were heated in the X-ray cell above the order−disorder transition temperature (T_{ODT}) or 250 °C, whichever was lower. Samples were subsequently cooled and held at a target temperature for 5−10 min prior to data collection. SAXS data are presented in two forms: I vs q or (Lorentz corrected) Iq^2 vs q, where I is the azimuthally integrated intensity and q is the scattering wave-vector modulus, $q = |\mathbf{q}| = 4\pi/\lambda \sin(\theta/2)$; λ is the wavelength and θ is the scattering angle. This type of data set is referred to as a 1D-SAXS pattern.

In addition, laboratory source small-angle X-ray scattering experiments were performed at the University of Minnesota Institute of Technology (IT) Characterization Facility. Cu Kα X-rays (λ = 1.54 Å) were generated using a Rigaku RU-200BHV rotating anode equipped with a 0.2 × 2 mm^2 microfocus cathode, and the beam was monochromated with total reflecting Franks mirror optics. The scattering data were collected with a Siemens HI-STAR multiwire area detector and corrected for detector response characteristics.

TEM. Transmission electron microscopy (TEM) was performed on a JEOL 1210 TEM operating at 120 kV, in the IT Characterization Facility at the University of Minnesota. Samples were heated under vacuum above T_{ODT} (up to a maximum of 250 °C), then cooled and held at 100−120 °C for 2−3 days, and then quickly cooled to room temperature. Sample slices, ≈70 nm thick, were cut at −80 °C using a Reichart Ultramicrotome fitted with a Microstar diamond knife. Microtomed sections were stained with the vapor from a 4% aqueous solution of OsO_4 for 3−10 min. This metal oxide selectively reacts with the olefinic groups present in the backbone of the PI blocks leading to contrast. The duration of staining was optimized to achieve adequate contrast based on the thickness of the sections and the proportion of the poly(isoprene) block in the materials.

DMS. Dynamic mechanical spectroscopy (DMS) experiments were conducted on a Rheometrics Scientific ARES strain-controlled rheometer using a 25 mm parallel plate fixture maintained at a gap of 1 mm under a nitrogen atmosphere. Samples were molded into 25 × 1 mm disks using 1000 psi at 100 °C for 5−10 min. Isochronal (ω = 1 rad/s) experiments were conducted while heating or cooling specimens at a rate of 1 °C/min. Discontinuous changes in the elastic (G') and loss (G'') moduli are indicative of morphological transitions. Isothermal frequency sweeps between $\omega = 10^2$ and 10^{-1} rad/s were conducted to probe the morphological response at specific temperatures; at low frequencies $G'(\omega)$ and $G''(\omega)$ are sensitive to the underlying morphology and state of order. All measurements were performed at low strain amplitudes of 1−2% that were determined to be within the linear viscoelastic regime.

Static Birefringence. Sample disks 10 mm in diameter by 1 mm thick were contained and sealed between two glass windows and placed between crossed-polarizing films in a temperature-controlled chamber. A beam of light from a 15 mW He−Ne laser was passed through this assembly, and the transmitted light intensity was monitored using a photodiode detector. The signal was normalized by the intensity recorded without a sample in the instrument and with the polarizing films arranged parallel to one another, which maximizes light transmission. The transmitted light intensity can be correlated with the symmetry of the specimen morphology.[41−43] Isotropic structures such as a disordered fluid or a cubic phase are not birefringent and therefore do not rotate light, resulting in little or no transmitted intensity. Noncubic ordered phases transmit a significant portion of the incident intensity.

Shear Alignment. Large strain amplitude reciprocating shear was applied to selected samples, in an apparatus described by Koppi et al.,[44] in order to macroscopically align isotropic ordered grains into a "single crystal". 1 mm thick sheets of polymer were compression-molded using 1000 psi at 100 °C for 5 min. After cooling, a portion was cut with dimensions of approximately 2 cm × 2 cm × 1 mm. Specimens were subjected to reciprocating shear for 2 h with a strain amplitude of 300% and shear rate of 0.55 s^{-1} while maintained at 200 °C under a nitrogen atmosphere. After

Table 1. ISO Triblock Characterization Data[a]

specimen	f_I	f_S	f_O	M_n (kg/mol)	M_w/M_n	phase	d (nm)[c]	T_{OOT} (°C)	T_{ODT} (°C)
IS-21	0.80	0.20	0.00	9.8	1.07	DIS			
ISO-21a	0.70	0.17	0.13	11.6	1.04	HEX → BCC	22.2	149	178
ISO-21g	0.67	0.16	0.17	12.3	1.05	HEX	15.6		226
ISO-21h	0.65	0.16	0.19	12.7	1.05	HEX	17.3		>250
ISO-21i	0.61	0.14	0.25	13.5	1.06	HEX	18.1		>250
ISO-21f	0.53	0.13	0.34	16.0	1.04	LAM	22.7		>250
ISO-21d	0.48	0.12	0.40	17.7	1.04	LAM	23.5		>250
ISO-21c	0.44	0.11	0.45	19.8	1.06	LAM	27.4		>250
ISO-21b	0.35	0.09	0.56	25.3	1.05	LAM	33.8		>250
ISO-21e	0.25	0.06	0.69	38.2	1.06	LAM	39.0		>250
ISO-8d[b]	0.56	0.27	0.17	22.0	1.05	HEX	22.5		>250
IS-20	0.64	0.36	0.00	9.2	1.08	DIS			
ISO-20a	0.52	0.29	0.19	11.8	1.06	HEX	17.1 (120)		240
ISO-20d	0.47	0.27	0.26	13.1	1.04	LAM	16.0		152
ISO-20g	0.44	0.26	0.30	14.0	1.11	LAM	16.2		>250
ISO-20c	0.37	0.20	0.43	17.6	1.16	LAM	18.3		>250
ISO-20e	0.31	0.18	0.51	20.8	1.12	Q^{230} → HEX	20.0	199	>250
ISO-20b	0.29	0.16	0.55	23.0	1.09	[LAM/HEX][e] → Q^{230}	53.4 (90)	159	>250
ISO-20f	0.21	0.11	0.68	32.8	1.09	HEX → BCC	34.1	130	244
IS-28	0.51	0.49	0.00	6.8	1.08	DIS			
ISO-28c	0.29	0.25	0.46	13.6	1.06	LAM	17.1 (120)		>250
ISO-28a	0.28	0.24	0.48	14.2	1.07	LAM	17.5		>250
ISO-28d	0.25	0.20	0.55	16.6	1.07	LAM	19.0 (120)		>250
ISO-28b	0.21	0.17	0.62	19.9	1.10	LAM → Q^{230}	53.9 (120)	146	>250
ISO-28e	0.19	0.14	0.67	23.1	1.09	[HPL] → Q^{230}	56.8	199	>250
ISO-28f	0.15	0.12	0.73	28.6	1.13	HEX	23.1		>250
IS-30	0.43	0.57	0.00	5.8	1.04	DIS			
ISO-30b	0.19	0.25	0.56	16.7	1.08	LAM → O^{70}	0.282, 0.556, 61.1 (220)[d]	155	192
ISO-30a	0.16	0.22	0.61	14.6	1.09	Q^{230}	40.7 (220)		174
IS-26	0.33	0.67	0.00	7.4	1.10	DIS			
ISO-26d	0.20	0.45	0.35	12.0	1.07	LAM	13.2		115
ISO-26a	0.19	0.39	0.42	13.7	1.11	LAM	14.3		157
ISO-26c	0.18	0.38	0.44	14.2	1.08	LAM	14.5		167
ISO-26b	0.16	0.33	0.51	16.4	1.10	LAM	15.9		185
ISO-26e	0.13	0.29	0.58	19.2	1.11	LAM → O^{70}	0.289, 0.591, 64.4 (180)[d]	139	196
ISO-26g	0.13	0.27	0.60	20.1	1.06	LAM → O^{70}	0.280, 0.554, 65.6 (160)[d]	103	201
ISO-26f	0.12	0.24	0.64	22.7	1.11	Q^{230}	42.9		202
IS-27	0.22	0.78	0.00	10.0	1.08	DIS			
ISO-27e	0.14	0.55	0.31	15.0	1.07	HEX	14.9 (90)		108
ISO-27a	0.12	0.44	0.44	18.8	1.10	LAM	16.6		171
ISO-27b	0.11	0.42	0.47	20.0	1.11	LAM	18.0		222
ISO-27c	0.10	0.40	0.50	21.2	1.11	LAM	19.3		238
ISO-27f	0.08	0.30	0.62	28.6	1.10	LAM	22.2 (140)		>250
ISO-27d	0.05	0.20	0.75	43.0	1.19	HEX	24.2 (110)		>250

[a] Lattice dimensions, d, calculated as $d = 2\pi/q^*$ are based on LAM [10], BCC [001], Q^{230} [001], and HEX [100] planes and for specimens having OOTs, and d corresponds to that of the high-temperature phase. Transition temperatures of T_{ODT} and T_{OOT} are based on data obtained during isochronal heating in DMS. [b] Synthesized by C. M. Hardy. [c] Measured at 100 °C unless mentioned in parentheses. [d] Corresponds to a/c, b/c, and c of orthorhombic unit cell at specified temperature. [e] [ ] indicates tentative assignment.

completion of shearing, the sample was cooled to room temperature at about 3−4 °C/min. A 1 mm^3 cubic section was cut from the aligned sheet, and the morphology of this section was analyzed with SAXS by directing the X-ray beam along each of the three orthogonal axes, defined by the shear geometry.

Results and Analysis

Forty-four ISO specimens, listed in Table 1, were synthesized with nearly monodisperse molecular weight distributions across a wide range of compositions. The overall molecular weights were designed to maintain the specimens within the limits of weak and intermediate segregation strength. Phase behavior was determined on the basis of SAXS, TEM, DMS, and birefringence experiments, between 90 and 250 °C, limited by the glass-transition temperature of polystyrene and thermal degradation. In this paper five ordered phase symmetries were identified as described in this section: lamellae (LAM), double gyroid (Q^{230}), *Fddd* orthorhombic (O^{70}), hexagonal (HEX), and body-centered cubic (BCC). (A sixth ordered cubic phase referred to as alternating gyroid or Q^{214} was reported earlier[12] and is included in the summary of ISO results presented in the Discussion section.) In order to establish the molecular parameters associated with each phase type, representative data sets and preliminary analyses are first presented followed by a summary diagram that establishes the overall composition dependence of each morphology.

For each category, we begin by assessing the order−disorder transition temperature, T_{ODT}, followed by an evaluation of possible order−order transition temperatures, T_{OOT}'s, both based on G' and G'' measurements. With the temperature range of likely ordered phases so bracketed, SAXS data are presented and diffraction peak positions are analyzed to establish phase symmetry. These represent our principal characterization tools. Selected TEM and birefringence measurements were employed to corroborate conclusions drawn from the SAXS experiments. Lattice parameters listed in Table 1 have been calculated on the basis of symmetry assignments and associated Bragg spacings determined by SAXS.

Lamellar Phase (LAM). Twenty-four of the specimens appearing in Table 1 were characterized as having a lamellar phase based on sharp diffraction peaks appearing in the SAXS

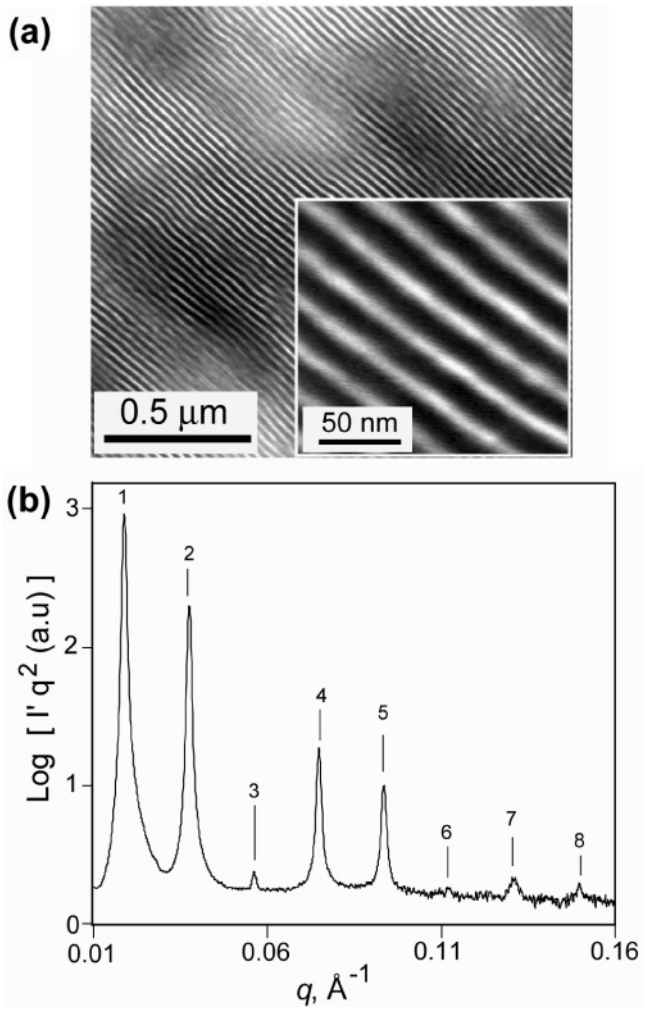

Figure 1. (a) TEM image from ISO-21b showing long-range lamellar (LAM) order. The dark regions are OsO_4 stained I-domains, and the light regions correspond to S- and O-domains. (b) Synchrotron SAXS pattern recorded from ISO-21b at 100 °C. Sequence of diffraction peaks is consistent with a LAM morphology. Background corrected scattering intensity, I', has been corrected by multiplication by q^2.

patterns at $q/q^* = 1, 2, 3, ...$, where q^* identifies the position of the first reflection. Between three and eight orders of diffraction were recorded indicative of various degrees of long-range order; in some instances higher order scattering was inaccessible due to the limited q range. DMS experiments, used to identify T_{ODT}, are not shown for brevity. Figure 1 shows TEM and SAXS data for representative specimen ISO-21b. In the TEM micrograph the adjacent S- and O-domains are indistinguishable since these do not stain with OsO_4, in contrast with the I-domains, which appear dark. We further analyze several of the lamellar SAXS patterns in the Discussion section.

***Fddd* Orthorhombic Network Phase (O^{70}).** Three specimens, ISO-26e, ISO-26g, and ISO-30b, were determined to contain the orthorhombic O^{70} phase;[12,28] here we present representative results from sample ISO-26g. Two phase transitions are suggested by changes in G' and G'' ($\omega = 1$ rad/s) while heating this material at 1 °C/min (Figure 2a). An order of magnitude increase in moduli beginning at 103 °C is indicative of an OOT while a discontinuous drop in elasticity at about 201 °C signals the ODT. Hysteresis in these mechanical properties upon cooling (Figure 2b) is consistent with first-order phase transitions; complete recovery of the low-temperature response was not obtained likely due to the proximity of the T_{OOT} to T_g for polystyrene. Isothermal frequency responses for this specimen in the low- and high-temperature regimes are qualitatively different as illustrated in parts c and d of Figure 2, respectively. For the high-temperature state, the dynamic moduli are solidlike ($G' \sim \omega^0$, $G' > G''$), typical of a triply periodic structure, while the low-temperature state is decidedly different, $G' \sim \omega^{0.2}$. Kossuth et al.[45] have shown that the low-frequency dynamic elastic modulus is very sensitive to the nature of the periodic order. For triply periodic morphologies such as gyroid and BCC spheres, $G' \sim \omega^0$, while cylinders and lamellae yield $G' \sim \omega^n$, where $1/4 \leq n \leq 1/2$.

SAXS data obtained from ISO-26g at various temperatures are shown in Figure 3. Samples were prepared by annealing the powdered specimen under vacuum at 100 °C for 2 h followed by cooling back to room temperature. For the first set of experiments, the sample was heated to a series of temperatures and annealed in each instance for 5 min prior to X-ray exposure. Figure 3 shows SAXS patterns recorded at 100, 160, and 220 °C. A single broad peak at the highest temperature is consistent with $T_{ODT} = 201$ °C, established by DMS. Reflections at 160 °C can be indexed with the *Fddd* space group consistent with an O^{70} phase assignment[12,28,46] (see following paragraph). Cooling from 220 to 140 °C leads to the same sequence of scattering peaks. Further cooling to 100 °C results in an additional pair of sharp peaks with relative q/q^* spacing of 1:2, superimposed on the high-temperature pattern. We interpret this result as deriving from a mixture of two phases, LAM and O^{70}. Upon reheating to 180 °C a scattering pattern consistent with *Fddd* symmetry is recovered, albeit with lower peak intensities than were recorded at 160 and 140 °C.

An expanded view of the SAXS pattern obtained from ISO-26g at 160 °C is presented in Figure 4. The diffraction peaks have been indexed on the basis of an orthorhombic unit cell with *Fddd* symmetry and dimensions $a/c = 0.280$, $b/c = 0.554$, and $c = 65.6$ nm. The allowed Miller indices for the *Fddd* space group, 004, 111, 022, 113, 115, 131, 026, 133, 040, 202, 220, and 222, are marked in this figure. Peaks corresponding to the 026 and 040 planes are not evident most likely due to coupled effects of structure factor and form factor on the scattering intensities. Here we note that slight variations in the unit cell dimensions can result in large changes in the locations of certain higher order peaks. The ratio of the unit cell dimensions a/c and b/c for O^{70} specimens identified in this study (see Table 1) are almost the same as those reported earlier for other ISO triblock copolymers exhibiting the O^{70} phase.[12]

Figure 5 shows the transmitted light intensity, obtained while heating and cooling ISO-26g in the birefringence apparatus between 80 and 210 °C at 1 °C/min. A relatively high transmitted intensity below 220 °C is indicative of optical anisotropy, consistent with the O^{70} and LAM phase assignments.[12,28,41,42] Extinction of recorded intensity above 200 °C with heating is consistent with a state of disorder. Even the hysteresis in G' and G'' reported in Figure 2a,b is reflected in the birefringence measurement around T_{ODT}.

Results similar to those associated with the O^{70} phase in ISO-26g were documented in ISO-26e and ISO-30b. In all three cases this phase lies adjacent to the disordered state, similar to our earlier findings.[12]

Double Gyroid Phase (Q^{230}). Specimens determined to have the double gyroid morphology (Q^{230}) included ISO-20e, ISO-20b, ISO-28e, ISO-26f, and ISO-30a. Representative results from the specimen ISO-26f are presented in this subsection. Figure 6 illustrates isochronal ($\omega = 1$ rad/s) and superpositioned isothermal G' and G'' traces for this material. A discontinuous

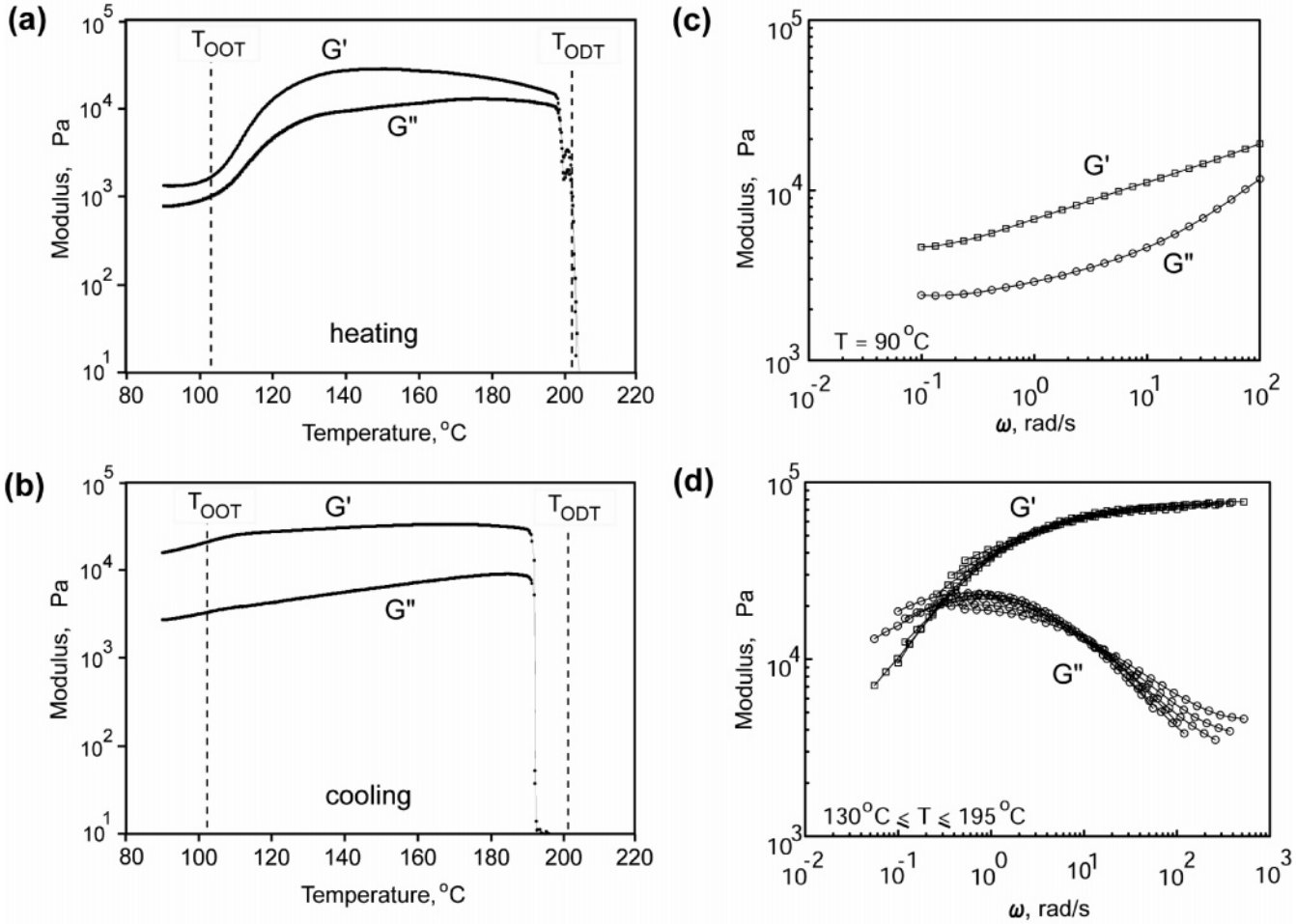

Figure 2. G' and G'' vs temperature for ISO-26g during isochronal (a) heating and (b) cooling, at 1 °C/min and $\omega = 1$ rad/s. Dashed lines correspond to order−order and order−disorder transition temperatures measured during heating. Superposition of isothermal frequency responses at (c) 90 °C and (d) temperatures between 130 and 195 °C.

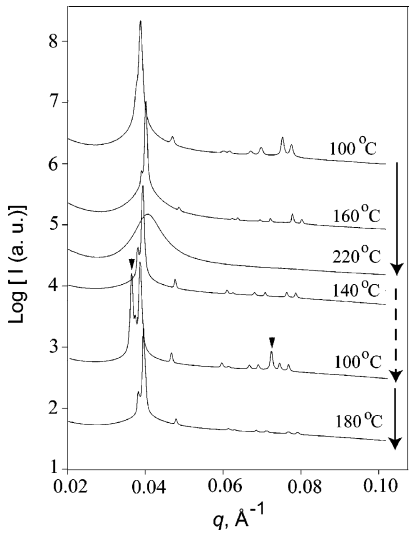

Figure 3. Synchrotron SAXS data for ISO-26g obtained while heating from 100 to 220 °C followed by cooling back to 100 °C and finally heating to 180 °C. The patterns are shifted vertically for clarity. Solid and dashed arrows indicate heating and cooling cycles, respectively. A single broad peak at 220 °C indicates disorder while scattering at all other temperatures is associated with the O^{70} phase. The scattering pattern obtained upon cooling to 100 °C is speculated to derive from coexisting O^{70} and LAM phases, where the triangular symbols locate first- and second-order Bragg peaks from a lamellar state.

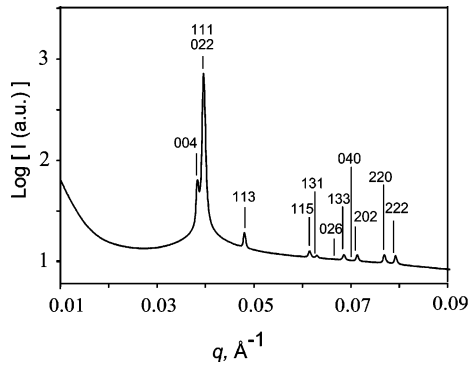

Figure 4. Bragg scattering from ISO-26g at 160 °C indexed according to *Fddd* space group symmetry, consistent with the O^{70} phase. The orthorhombic unit cell dimensions are listed in Table 1.

drop in both moduli upon heating, and redevelopment of solidlike properties with hysteresis upon cooling, evidence a single ordered morphology with triply periodic structure between 90 and 202 °C. SAXS experiments provided unequivocal evidence that this state contains $Ia\bar{3}d$ space group symmetry, which is well established to be associated with the double gyroid morphology.[12,13,47] An example scattering pattern is presented in Figure 7. Reflections are apparent at relative positions $q/q^* = \sqrt{6}, \sqrt{8}, \sqrt{14}, \sqrt{16}, \sqrt{20}, \sqrt{22}, \sqrt{24}$, and $\sqrt{26}$, all consistent with $Ia\bar{3}d$ symmetry; an allowed reflection at $\sqrt{14}$ is not resolved. Also, an approximately 10 to 1 ratio in intensity between the first (211) and second (220) Bragg peaks is consistent with this assignment.[47] Other SAXS experiments conducted with this group of specimens displayed additional

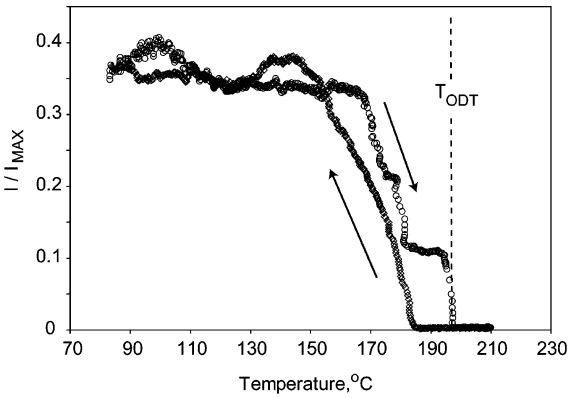

Figure 5. Birefringence measurements from ISO-26g during heating and cooling at 1 °C/min. Transmitted intensity at low temperatures is consistent with O[70] and LAM phases as indicated by SAXS measurements.

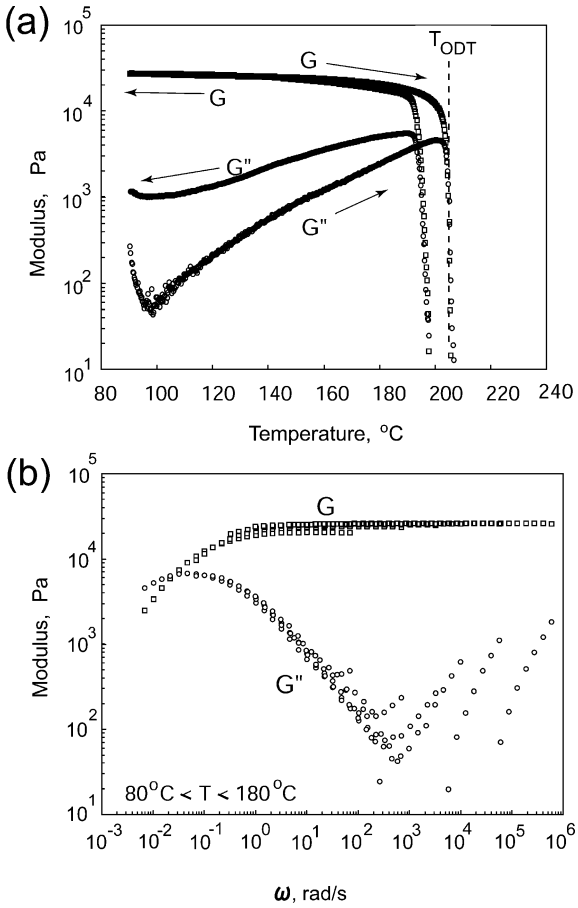

Figure 6. (a) G' and G'' for ISO-26f during heating and cooling at 1 °C/min and $\omega = 1$ rad/s. (b) Superposition of isothermal frequency traces obtained between 80 and 180 °C in increments of 20 °C. These results are indicative of triply periodic (i.e., solidlike) order, consistent with the SAXS-based Q[230] phase assignment.

intensity maxima at $\sqrt{32}$, $\sqrt{38}$, $\sqrt{40}$, $\sqrt{42}$, $\sqrt{46}$, $\sqrt{48}$, and $\sqrt{50}$ (not shown here), all allowed by the $Ia\bar{3}d$ symmetry.

Birefringence measurements (Figure 8) were performed on specimen ISO-26f to reinforce the cubic phase assignment. Aside from a small amount of birefringence recorded between 90 and 120 °C during the initial heating of the specimen (we attribute this to residual stress that relaxes as the material passes through the glass transition), this triblock copolymer is optically isotropic at all measurement temperatures during heating and cooling. No evidence of the ODT is apparent, consistent with

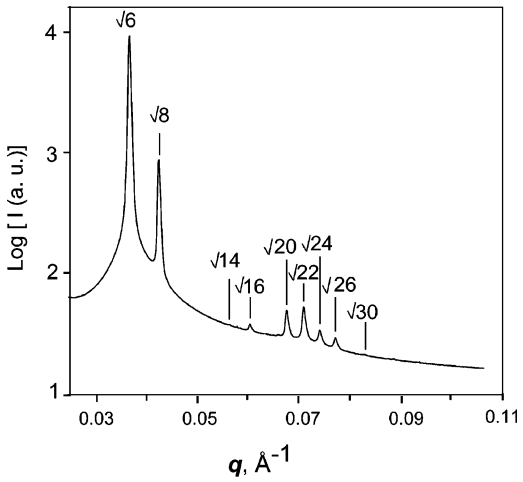

Figure 7. Synchrotron SAXS data for ISO-26f at 180 °C. The peaks are indexed with $Ia\bar{3}d$ space group symmetry, associated with the Q[230] phase.

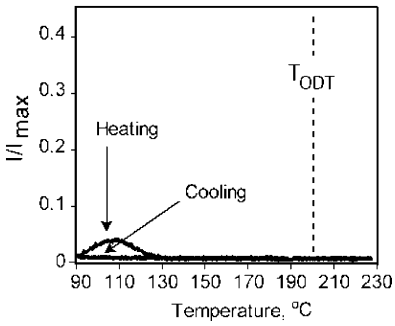

Figure 8. Birefringence results for ISO-26f during heating and cooling at 1 °C/min. The dashed line indicates T_{ODT} as determined by DMS. Lack of transmitted intensity is consistent with isotropic cubic and disordered phases. The small amount of birefringence at low temperatures is attributed to initial heating through the glass transition.

a thermodynamic transition between two nonbirefringent states, i.e., cubic and disordered.[12,41,42]

Hexagonal Phase (HEX). Eleven ISO triblocks (ISO-21a, -21g, -21h, -21i, -20a, -20e, -20b, -20f, -28f, -27d, and -8d) from Table 1 were determined to contain hexagonal ordered symmetry. These specimens can be grouped within three different composition regions and DMS and SAXS data for three representative specimens ISO-21h, ISO-27e, and ISO-28f are shown in Figures 9 and 10, respectively.

The superposed isothermal frequency DMS results (Figure 9) for each specimen were decidedly not solidlike, suggesting that the underlying state of order is either singly or doubly, but not triply, periodic. In each case the Bragg peaks appearing in the associated SAXS patterns (Figure 10) are indexed with relative peak locations at $q/q^* = \sqrt{1}$, $\sqrt{3}$, $\sqrt{4}$, $\sqrt{7}$, $\sqrt{9}$, $\sqrt{12}$, and $\sqrt{13}$, consistent with hexagonal symmetry.

Specimen ISO-28f was subjected to a reciprocating shear as explained in the Experimental Section, and a small cubic section was cut for further analyses. This piece of material was held at 40 °C while it was irradiated with the collimated laboratory X-ray source directed along three orthogonal directions coordinated with respect to the applied shear, as sketched in Figure 11. This figure also shows the resulting 2D scattering patterns, along with azimuthal plots of I vs φ ($0 \le \varphi \le 360°$), integrated over the radial distance $q^* \pm 0.012$ Å^{-1}. Arcs of intensity centered on q_y^* and q_z^* along with a weak but clearly established set of six hexagonally placed intensity maxima in the $q_y - q_z$ plane indicate a cylindrical morphology aligned with the long axis coincident with the direction of shear.

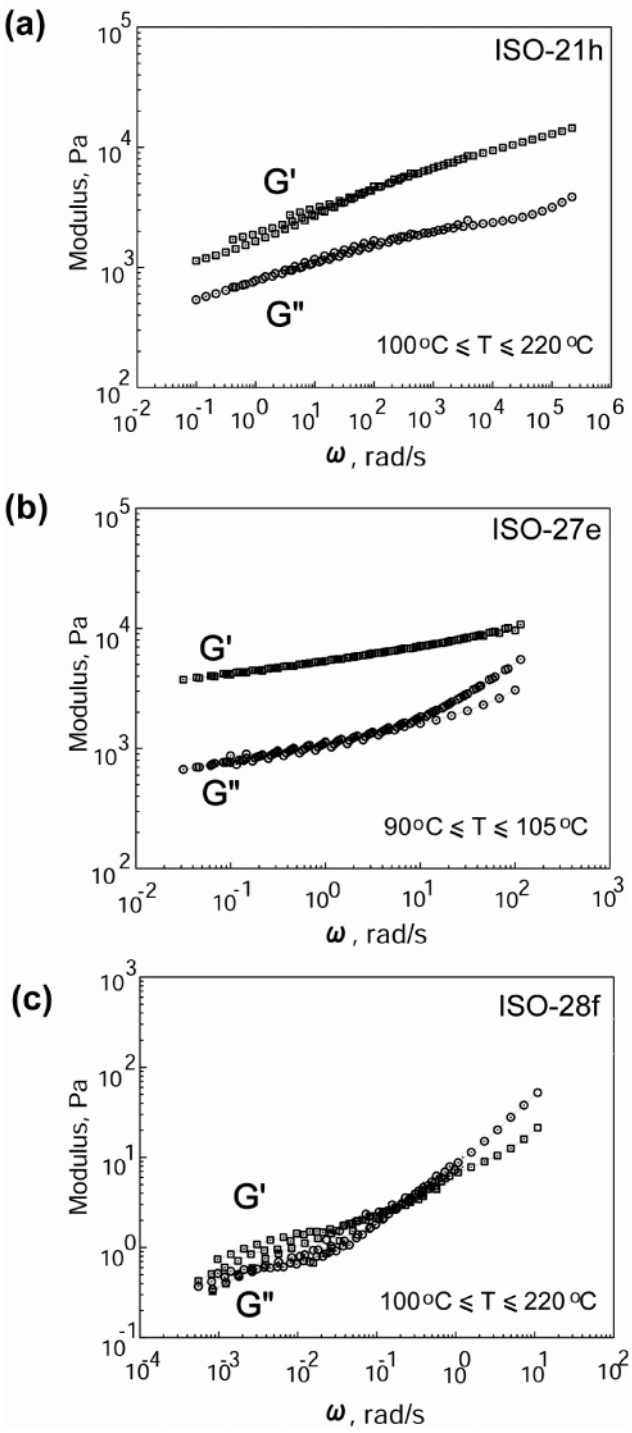

Figure 9. Superposed isothermal G' and G'' traces with varying frequency for (a) ISO-21h, (b) ISO-27e, and (c) ISO-28f. These results are indicative of underlying morphologies with singly or doubly periodic order.

A TEM image taken from a thin section of the shear aligned ISO-28f specimen is presented in Figure 12. We discovered that finding long-range order in this and other samples exhibiting hexagonal symmetry, and containing a majority of PEO, was not possible. Nevertheless, in selected locations we could make out local 6-fold symmetry as highlighted in the inset to Figure 12. We attribute the apparent disorder in this and other specimens to crystallization of PEO during cooling, which is known to be disruptive to ordered microstructure in certain block copolymers.[48] ISO-28f contains just 12% PS, likely mixed to some extent with both PEO and PI in the melt state. Under these conditions it seems unlikely that vitrification of PS would restrain the disruptive effects of PEO crystallization. This deduction is supported by the SAXS patterns for ISO-28f shown in Figure 10; prior to measurement the sample had been cooled from 160 to 40 °C. Just two broad peaks at 40 °C are consistent with local microdomain correlations but a lack of long-range order. Heating this specimen to 100 °C leads to recovery of at least five considerably sharper diffraction peaks, representative of the hexagonally ordered melt state.

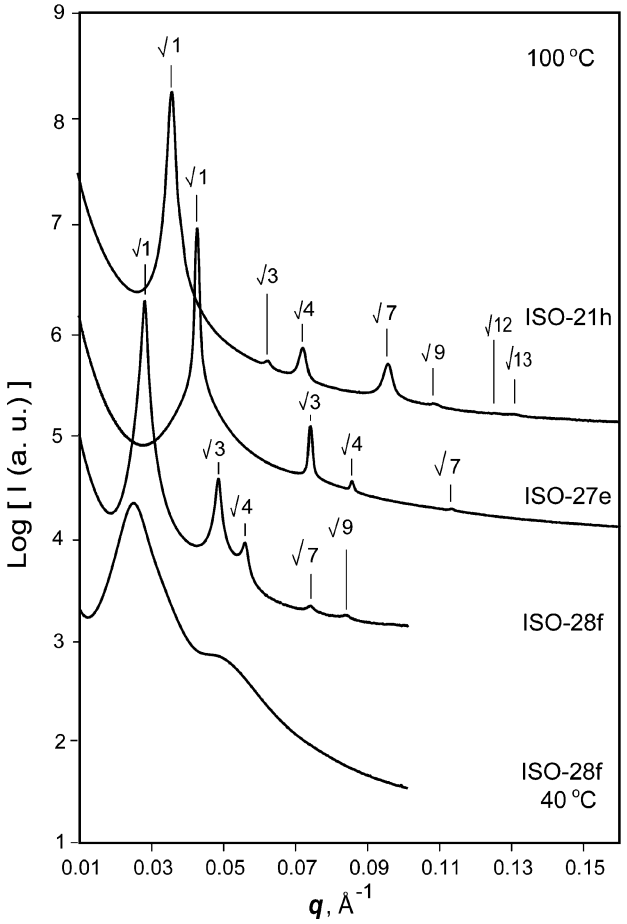

Figure 10. Synchrotron SAXS data obtained at 100 °C for specimens ISO-21h, ISO-27e, and ISO-28f (top curve), each indexed based on hexagonal symmetry. The pattern for ISO-28f at 40 °C illustrates the consequences of cooling below the crystallization temperature for PEO. The patterns are shifted vertically for clarity.

Body-Centered Cubic Phase (BCC). Two triblocks, ISO-20f and ISO-21a, were determined to have a stable BCC state. Both specimens displayed order−order transitions (see Table 1) where the BCC state was the highest temperature ordered phase bordering the ODT. Figure 13 shows isochronal (heating and cooling) and superposed isothermal frequency DMS results for sample ISO-20f. Evidence of a morphological transition between 115 and 130 °C is most apparent in G'', and less so in G', as the material was heated from 80 °C through $T_{ODT} \approx 244$ °C. The low-temperature state does not appear to be recovered upon cooling, perhaps due to the finite rate of cooling compounded by vitrification of poly(styrene). The viscoelastic response of the high-temperature phase between 160 and 235 °C suggests a triply periodic state of order, similar to that found in Figures 2d and 6b.[45,49]

SAXS patterns obtained at 160 and 100 °C from ISO-20f are presented in parts a and b of Figure 14, respectively. At the higher temperature, Bragg diffraction provided peak intensities at relative wavevectors $q/q^* = \sqrt{2}, \sqrt{4}, \sqrt{6}, \sqrt{8}, \sqrt{10}, \sqrt{12},$

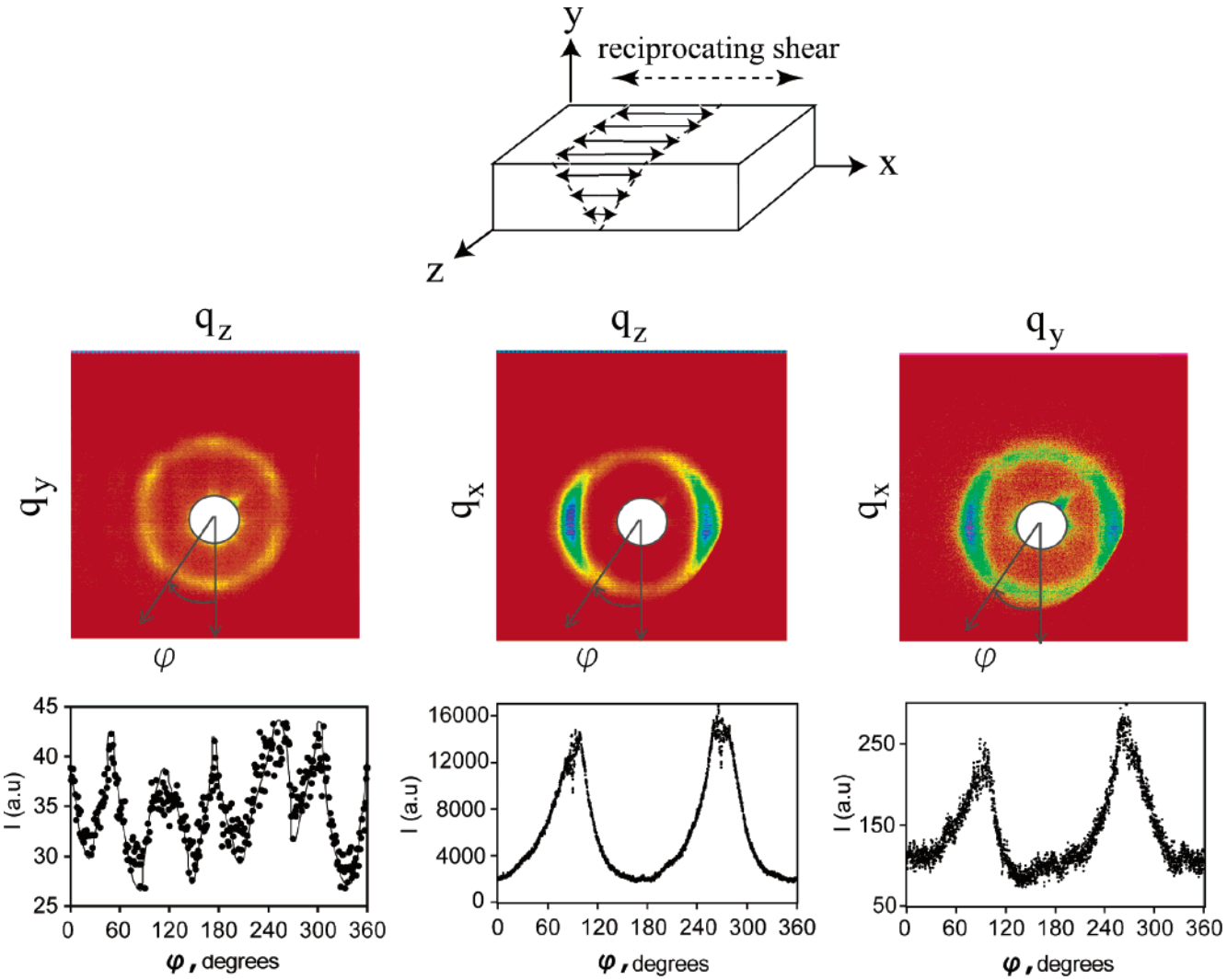

Figure 11. 2D-SAXS patterns obtained from ISO-28f following large-amplitude (300%) reciprocating shear alignment. The sketch identifies the deformation coordinate system, where *x*, *y*, and *z* correspond to the velocity, gradient, and vorticity directions respectively. For each case integrated intensities over radial distance $q^* \pm 0.012$ Å^{-1} are plotted as a function of azimuthal angle. These results reinforce assignment of hexagonal symmetry and are consistent with a cylindrical morphology.

and $\sqrt{14}$, uniquely consistent with the allowed reflections for the $Im\bar{3}m$ space group. We assume this corresponds to the BCC placement of spherical microdomains. At the lower temperature three (possibly four) diffraction peaks were recorded at positions $q/q^* = \sqrt{1}$, $\sqrt{3}$, ($\sqrt{4}$), and $\sqrt{7}$, consistent with hexagonal (HEX) symmetry. However, transformation to the lower temperature state is accompanied by significant peak broadening indicative of a loss of long-ranged order.

Intermediate States. Two specimens exhibited order−order transitions with the double gyroid state at higher temperature and tentatively assigned states at lower temperature: hexagonally perforated layers (HPL) for ISO-28e and LAM/HEX mixture for ISO-20b.

Figure 15 shows isochronal DMS results for ISO-28e. While heating, the steep increase in G' at ∼200 °C and the undulating profile of G'' are indicative of an order−order transition. During cooling, the profiles are markedly different: G' remains high, and G'' does not display any discontinuous changes.

SAXS patterns are shown in Figure 16a at various temperatures. Data obtained while heating from 100 to 200 °C could not be indexed with any of the symmetries considered to this point. At 100 °C three peaks are evident at $q/q^* = 1$, 2, 3 along with three additional peaks at $q/q^* = 1.07$, 1.74, 2.16. Heating to 240 °C produces a dramatic change to a SAXS pattern clearly consistent with the Q^{230} state. Upon cooling, this pattern persists with a 7% dilation in the unit cell spacing at 90 °C relative to 240 °C. These results are consistent with the DMS data shown in Figure 15.

There are important differences in how we analyze the transition phenomena for specimen ISO-28e as opposed to that for ISO-26g (Figure 2) and ISO-20f (Figure 13). In all three materials the isochronal G' data are continuous when the specimen is cooled from the high-temperature state to the low-temperature state. However, unlike with ISO-26g and ISO-20f, the transition temperature for ISO-28e (∼199 °C) is much higher than T_g, eliminating the effects of vitrification as an explanation for the persistence of the high-temperature state. Furthermore, when ISO-26g and ISO-20f are cooled below the T_{OOT}, SAXS results indicate that the low-temperature states begin to form. In the case of ISO-26g there are SAXS peaks that derive from the coexisting lamellar grains, which are located by triangular symbols in Figure 3. ISO-20f produced broad peaks shown in Figure 14b. In contrast, SAXS results for ISO-28e indicate a complete absence of the low-temperature state. We speculate that this nonrecoverable intermediate state of ISO-28e is metastable. Additional SAXS experiments, conducted after longer annealing times, would be useful for clarifying the true thermodynamic state of this material.

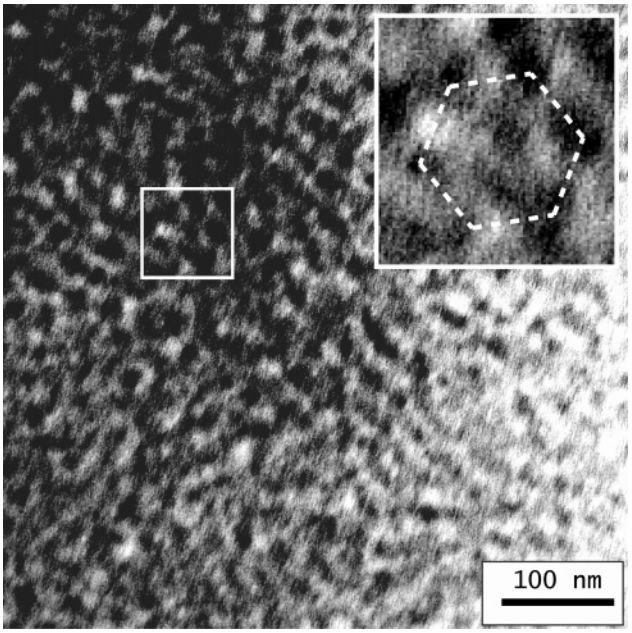

Figure 12. TEM image obtained from a section cut from a sheet of ISO-28f, after shear alignment. The image displays a lack of long-range order, but with only regions of short-range 6-fold symmetry as shown in the inset.

We have tentatively assigned the low-temperature state between 100 and 160 °C as hexagonally perforated layers (HPL). The Bragg peaks recorded at 160 °C can be accounted for by the space group $R\bar{3}m$ (Figure 16b). The HPL morphology with a ABCABC perforation stacking sequence is associated with the $R\bar{3}m$ space group.[50] At low temperatures (e.g., 100 °C) the reflections at integral spacing become more prominent consistent with a weakening of the in-plane hexagonal modulation, thus favoring lamellar symmetry. Moreover, the occurrence of HPL as a metastable state during morphological transitions to and from the double gyroid phase has been documented in the literature.[48,50−56]

Next we analyze results for ISO-20b shown in Figure 17. At the lowest measurement temperature, 33 °C, a SAXS pattern nearly devoid of discernible Bragg diffraction was recorded. We attribute this state of relative disorder to the effects of PEO crystallization as noted earlier. At higher temperature, between 90 and 220 °C we obtained well-defined scattering patterns that fall into two categories. Upon heating from 90 to 160 °C seven narrow peaks were recorded at relative spacings inconsistent with any identifiable space group symmetry. However, these results can be split into two groups, with relative spacings $q/q^* = 1, 2$ (triangular symbol) and $q/q^* = \sqrt{1}, \sqrt{3}, \sqrt{4}, \sqrt{7}, \sqrt{9}$ (lines). We associate these patterns with a mixture of lamellar and hexagonal (possibly cylindrical) symmetry.

Heating between 180 and 220 °C and subsequent cooling to 90 °C results in diffraction unambiguously associated with $Ia\bar{3}d$ symmetry, hence a Q[230] phase assignment. This sequence of scattering results resembles those obtained for ISO-28e, i.e., a nonrecoverable low temperature state likely reflecting a kinetically constrained, nonequilibrium state. We believe that melting of the PEO leads to spontaneous ordering, trapping both lamellae and cylinders in a metastable configuration. Heating either drives this arrangement unstable or facilitates nucleation of the gyroid phase. Once formed, the gyroid remains stable down to the PEO crystallization temperature. Similar behavior has been recorded with diblocks in the vicinity of the lamellar−cylinder transition.[57]

Poly(isoprene-*b*-styrene-*b*-ethylene oxide) Phase Map. Using the methods outlined in the previous paragraphs, we have

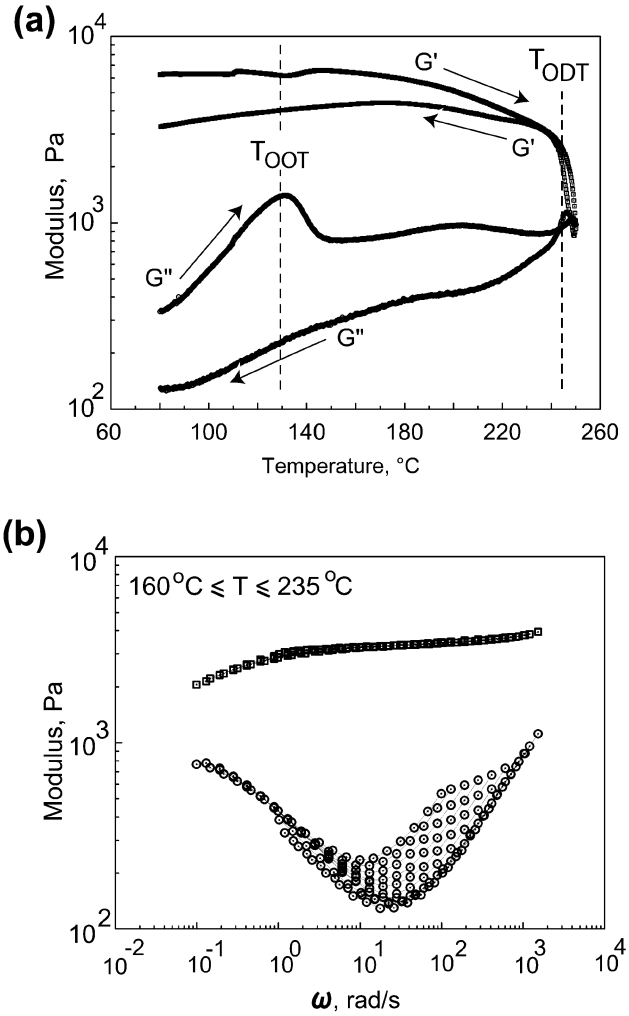

Figure 13. (a) G' and G'' for ISO-20f while heating and cooling at 1 °C/min and at a constant frequency of $\omega = 1$ rad/s. The dashed lines locate the ODT and OOT. (b) Superposed isothermal frequency traces recorded at various temperatures between 160 and 235 °C. This solidlike behavior is consistent with the BCC phase assignment established by SAXS.

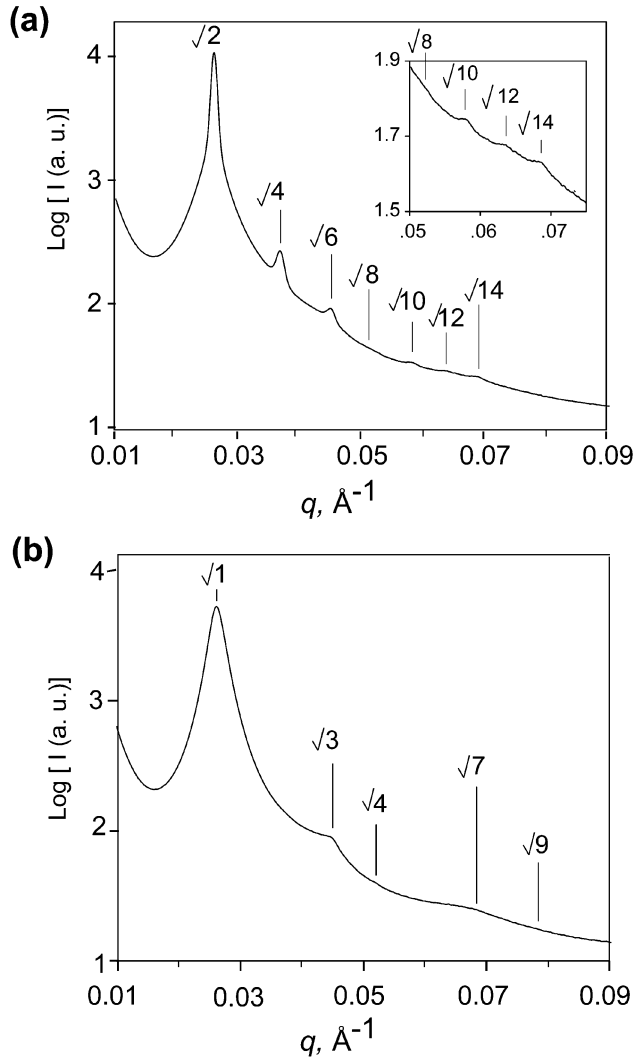

Figure 14. Synchrotron SAXS data for ISO-20f at (a) 160 and (b) 100 °C. The peak locations in (a) are consistent with $Im\bar{3}m$ (BCC) space group symmetry, while those in (b) can be indexed according to hexagonal symmetry.

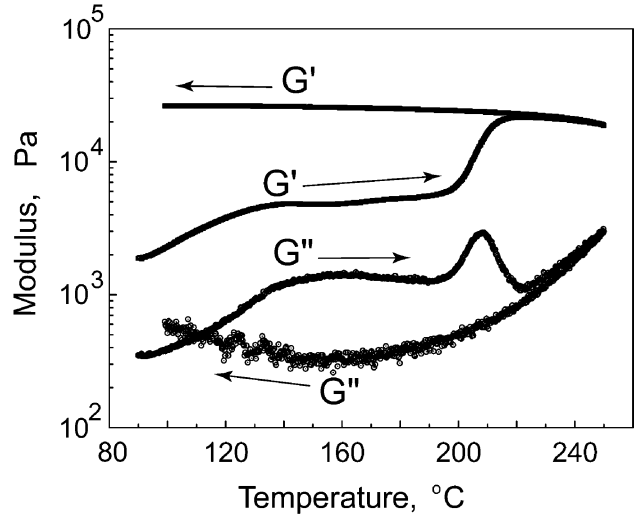

Figure 15. Isochronal (ω = 1 rad/s) DMS results for ISO-28e. The specimen was first heated from 90 to 250 °C and then cooled back to 90 °C at 1 °C/min.

assigned phase symmetries to all the specimens listed in Table 1. A three-dimensional phase map summarizing these results is

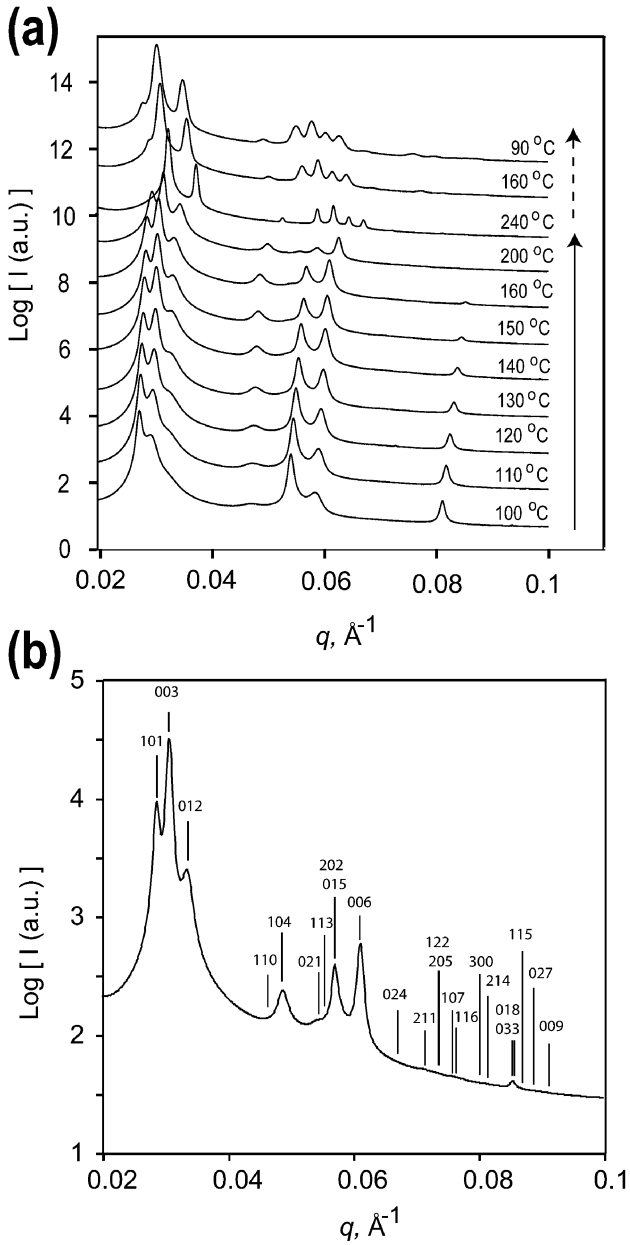

Figure 16. (a) Synchrotron SAXS data obtained while heating (100−240 °C) and then cooling (to 90 °C) ISO-28e. The patterns are shifted vertically for clarity. (b) SAXS pattern at 160 °C, indexed according to space group $R\bar{3}m$ with lattice parameters: a = 50.4 nm and c = 114.9 nm. These results are interpreted to derive from a high-temperature Q^{230} phase and (tentatively) a metastable HPL phase at low temperature after heating from crystalline PEO.

depicted in Figure 18; this illustration includes results reported previously by Epps et al.,[12] bringing the total number of different ISO polymers evaluated by our group to 87. Figure 18 represents a projection of all our results obtained between 90 and 250 °C. In the event that a triblock displays an OOT that data point contains two colors identifying each ordered state symmetry.

Overall, the phase map locates clusters of common data points that reflect certain ordering tendencies. Lamellae dominate the central portion of the map extending from left to right across the entire triangle, i.e., from symmetric IO diblocks to symmetric SO diblocks. Double gyroid appears in two places, in the O-lean and O-rich parts of the illustration. O^{70} also is found in the O-lean and O-rich parts of the map but appears to be considerably more prevalent toward the IS boundary. This network phase was identified in the present work in just three specimens

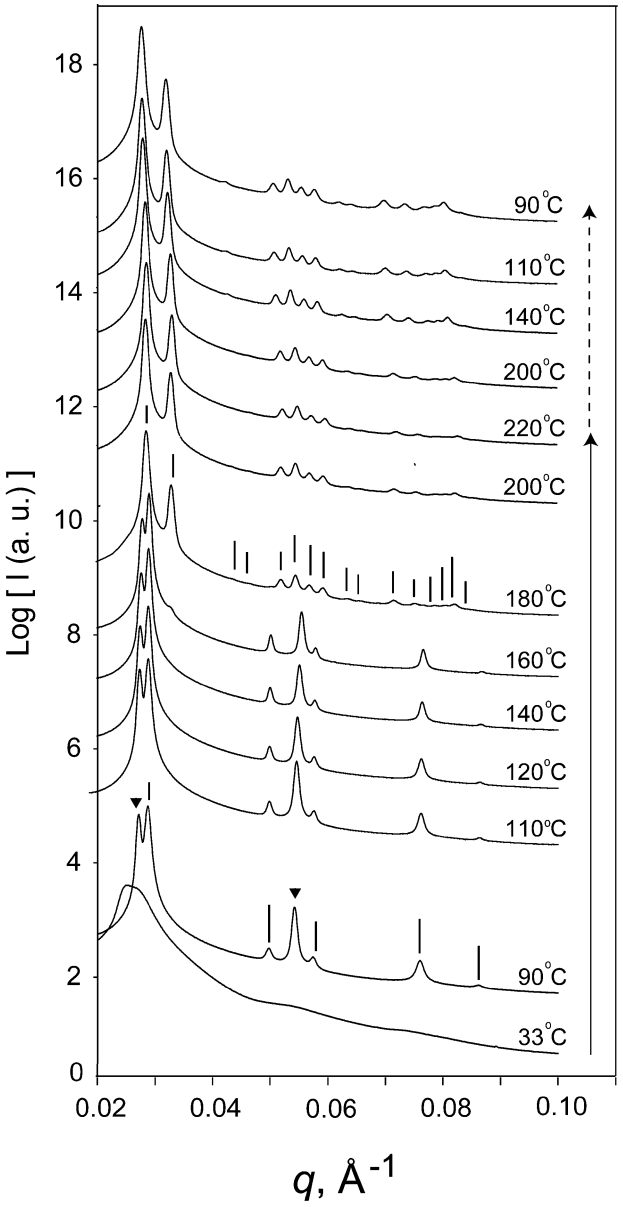

Figure 17. Synchrotron SAXS data from ISO-20b obtained while the specimen was heated from 33 to 220 °C and then cooled to 90 °C. The pattern at 90 °C obtained after heating from the crystalline PEO state is indexed as a mixture of LAM (triangular symbols) and HEX (lines). At high temperatures a Q^{230} phase is indicated as indexed at 180 °C. Solid and dashed arrows indicate heating and cooling, respectively. The patterns are shifted vertically for clarity.

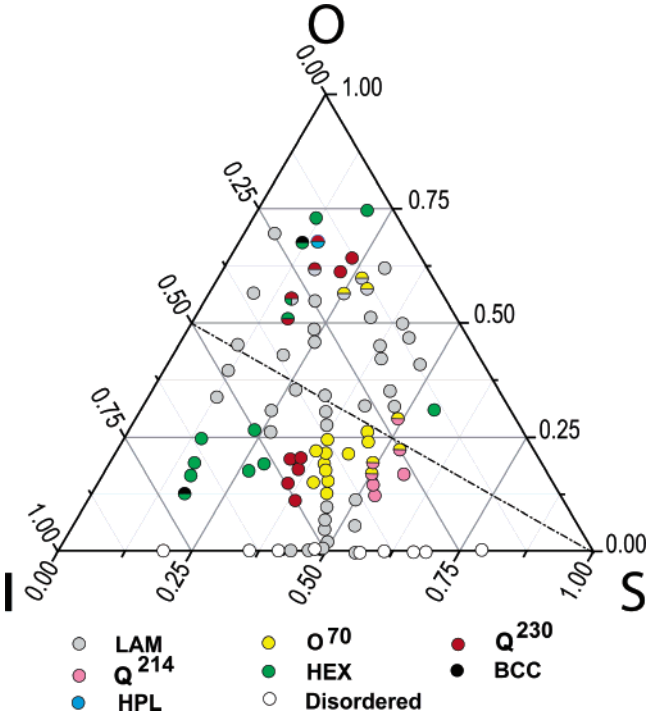

Figure 18. Phase map for poly(isoprene-*b*-styrene-*b*-ethylene oxide). The axes identify volume fractions of each block. Symbols identify phase behavior of ISO triblock specimens, including the results reported by Epps et al.[12] Phase assignments are identified by color as noted below the triangle. Six stable ordered phases, LAM (lamellar), HEX (hexagonal), Q^{230} (double gyroid), Q^{214} (alternating gyroid), BCC (body-centered cubic), O^{70} (*Fddd* orthorhombic network), the disordered state, and one metastable phase, HPL, are included. Specimens with order−order transitions are shown with multicolored symbols with top and bottom halves representing high- and low-temperature states, respectively. The dashed line corresponds to the $f_I = f_O$ isopleth.

(around $f_O \approx 0.6$ and $f_I \approx 13-19\%$) and only at elevated temperatures; LAM was found at lower temperatures in each instance. Hexagonal symmetry is evident in three locations: I-rich, O-rich, and S-rich. Interestingly, the alternating gyroid phase, Q^{214}, was not seen in the present study. This network morphology was identified earlier straddling the $f_I = f_O$ isopleth toward the S-rich portion of the triangular map. Finally, two specimens displayed BCC symmetry at relatively low S content, $f_S \approx 0.11$ and 0.17, at high and low I_O; in both cases the BCC phase was sandwiched between hexagonal symmetry and disorder.

Discussion

ISO Phase Map. Currently, there is no universal theoretical or empirical treatment that captures the general phase behavior of ABC triblock copolymers. This places severe synthetic demands on the experimentalist aiming to produce a specific morphology from a given set of monomers. We embarked on this research program intending to provide a comprehensive set of results that would aid in the development of self-consistent mean-field theory (SCFT) for broader use. Tyler and Morse have taken the first exciting steps in this direction, demonstrating that the channel of three network phases (Q^{230}, O^{70}, and Q^{214}) located on the lower portion of Figure 18 can be accounted for by the statistical theory.[58]

ABC systems can be classified based on the relative magnitudes of the binary interaction parameters. For ISO the following temperature-dependent binary Flory−Huggins parameters have been reported:[59]

$$\chi_{IS} = 26.4T^{-1} - 0.0287$$
$$\chi_{SO} = 29.8T^{-1} - 0.0229$$
$$\chi_{IO} = 90.0T^{-1} - 0.0579 \quad (1)$$

based on a common segment volume of 118 Å^3. Thus, at 150 °C $\chi_{IS} = 0.034$, $\chi_{SO} = 0.048$, and $\chi_{IO} = 0.155$. Within reasonable uncertainty these values satisfy the inequality

$$\chi_{IO} > \chi_{IS} \approx \chi_{SO} \quad (2)$$

guaranteeing that microphase separation results in only two interfaces; i.e., an S-domain will always separate I- and O-domains. This class of triblocks has been referred to as "nonfrustrated"[60] since the block sequence "ISO" and thermo-

dynamically preferred placement of interfaces are self-reinforcing. In contrast, SIO triblocks are "frustrated" since O blocks least favor contact with I blocks but are forced to do so due to the molecular architecture; such systems tend to form morphologies containing three types of interfaces. We originally selected the ISO system in order to enhance the possibility of finding triply continuous network phases, which tend to be stabilized by nonintersecting interfaces.

If eq 2 was strictly applicable, and if the I and O chains were characterized by identical statistical segment lengths, then we would expect the phase map to be symmetric around the $f_I = f_O$ isopleth (dashed line in Figure 18). Apparently, this is not the case. The window of network phases occurs asymmetrically around this isopleth and is less extensive on the O-rich side vs the O-lean side. Moreover, we find no evidence of the alternating gyroid near the Q^{230} and O^{70} regions at higher O content. We attribute these asymmetries to the aforementioned differences in statistical segment lengths ($b_I = 6.07$ Å, $b_S = 5.47$ Å, and $b_O = 7.80$ Å based on a common segment volume of 118 Å^3)[40] along with differences between χ_{IS} and χ_{SO} at all temperatures. Apparently, the overall free energy of the individual morphologies is quite sensitive to the balance between these parameters. Recent calculations by Tyler and Morse seem to support this conjecture.[58,61] They have found that rather subtle variations in the interaction parameters dramatically affect the distribution of phases as a function of composition in the ternary phase map. Establishing quantitatively how these factors influence phase stability must be tackled with the SCFT. The results summarized in Figure 18 should be quite useful in validating such calculations.

Two other attractive nonfrustrated model triblock copolymer systems have been evaluated in earlier studies. Poly(styrene-*b*-isoprene-*b*-dimethylsiloxane) (SID) (and the frustrated version ISD) is characterized by relatively symmetrically distributed interaction parameters leading to similar end-block/center-block interfacial tensions.[62,63] Moreover, the blocks in this compound are either glassy (S) or rubbery (I and D) at room temperature facilitating TEM and SAXS experiments at ambient conditions. Another material with commercial potential is poly(cyclohexane-*b*-ethylethylene-*b*-ethylene) (CE_EE), prepared by catalytically hydrogenating unsaturated poly(styrene-*b*-1,2-butadiene-*b*-1,4-butadiene). Cochran and Bates have shown that this material also supports the O^{70} phase, at roughly the same composition as found with ISO, based on detailed synchrotron X-ray scattering experiments.[11] CE_EE and related saturated hydrocarbon multiblock copolymers are very attractive at possible commodity plastics and elastomers. However, small differences in electron density between C, E_E, and E, and poor inherent contrast, offers limited opportunities for SAXS and TEM, respectively. Nevertheless, SID and CE_EE, both nonfrustrated molecular architectures, support the notion that triblock copolymer phase behavior follows certain universal patterns.

Domain Mixing in LAM. Until this point in the presentation we have treated ISO phase behavior in a manner that implies that the blocks are segregated into three distinct subdomains. As is well established with AB diblock copolymers, there are two limiting, and one intermediate, states of segregation: weak (WSL), intermediate (ISL), and strong (SSL). Weak segregation implies sinusoidal-like variations in composition and applies to the disordered regime and the ordered state close to the ODT. In strong segregation the composition plateaus at essentially pure polymer levels within the subdomains, leading to composite behavior that reflects the properties of the individual blocks. Intermediate segregation implies local periodic concentrations that approach those of the pure blocks, with a sizable fraction of the material mixed at the domain interfaces.[64]

ABC triblocks are more complicated due to the possibility of asymmetric segment−segment interactions and two independent composition variables. In fact, it is important to keep in mind that these are single-component materials that support only a single thermodynamic phase as a function of temperature at fixed pressure. (Often the microdomain spaces are referred to as "phases", a misleading practice. For this reason, we refer to the diagram in Figure 18 as a phase map, not a phase diagram.) As the composition and molecular weight are varied across Figure 18, the segregation strength varies within the ISL. Provided the symmetry of the morphology remains fixed, it should be possible to characterize how the composition modulates across the phase map.

To probe the effect of segregation and mixing in the ISO triblocks, we have analyzed the SAXS results for different specimens present in the band of LAM materials stretching from the IO diblock side to the SO diblock side of Figure 18. TEM analysis is ambiguous for determining the state of segregation in ISO because S- and O-domains are both unstained and hence indistinguishable.

The triblock chains will be arranged periodically in a −ISO−OSI− sequence, resulting in a centrosymmetric stacking of domains. On the basis of eq 2, the likelihood of mixing I and O end blocks compared to that of mixing of S- with I-domains and I- with S-domains is exceedingly small. Changing the degree of segregation does not affect the centrosymmetric character of the lamellar stacking. To a first (crude) approximation, three limiting types of segregation are considered: (i) I−S−O having well segregated I-, S-, and O-domains, (ii) (I/S)-O with mixed I- and S-domains segregated from the O-domain, and (iii) I-(S/O) having mixed S- and O-domains segregated from the I-domain.

The strategy employed in this study relies on the relative intensities of the SAXS diffraction peaks, which depend upon the composition and the state of segregation and extent of long-range order. Since we have no information regarding the state of translational order, we assume perfect long-range order. Simple rectangular (box) models of electron density that account for the three crude states of lamellar segregation indicated in the previous paragraph are employed to generate simulated diffraction patterns for comparison with the experimental results.[65,66] Thus, the electron density of each domain, E^M, is a step-function of distance x in the direction perpendicular to the lamellae with the magnitude of each step (or domain) equal to the difference in electron density from that of the bulk average $\langle E \rangle$. The periodic length L corresponds to one ISOOSI repeat unit. The assumptions of the model are (i) the domain sizes are proportional to volume fraction of each block in the triblock chains, f_i; (ii) the interfaces are sharp; and (iii) the lattice is infinite and without defects and the stacking is centrosymmetric. The rectangular model for a perfectly segregated I−S−O state is

$$E^M(x) = \begin{cases} E^O - \langle E \rangle & -f_O(L/2) \le x \le f_O(L/2) \\ E^S - \langle E \rangle & f_O(L/2) < x \le (f_O + f_S)(L/2) \text{ and } -(f_O + f_S)(L/2) \le x < -f_O(L/2) \\ E^I - \langle E \rangle & (f_O + f_S)(L/2) < x \le L/2 \text{ and } -L/2 \le x < -(f_O + f_S)(L/2) \end{cases} \quad (3)$$

Other states of segregation that were considered were that of the S-domain being partially mixed with either I- or O-domains, that is, going from a fully segregated I−S−O triblock to essentially (I/S)-O or I-(S/O) diblocks, by gradual mixing the

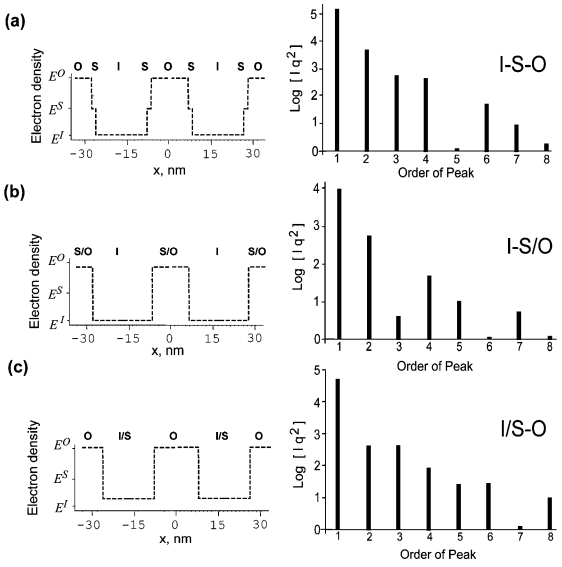

Figure 19. Rectangular models and calculated diffraction for lamellar segregation based on the composition of ISO-21b. The models represent three limiting cases: (a) well segregated I-, S-, and O-domains, (b) mixed I- and S-domains segregated from the O-domains, and (c) mixed S- and O-domains segregated from I-domains. Intensity profile in (b) is most consistent with the experimental SAXS results shown in Figure 1b.

S-domain with I- and O-chains, respectively. The domain sizes and the relative magnitudes of the electron densities were adjusted according to these mixing schemes. Since the periodic system is centrosymmetric, the diffraction amplitudes, A_n^M, of the nth order diffraction peaks can be calculated by inverse Fourier transformation of the model, $E^M(x)$

$$A_n^M = \frac{2}{L}\int_0^L E^M(x)\cos\left(\frac{2\pi n x}{L}\right)\mathrm{d}x \quad (n > 0) \tag{4}$$

where the peak intensities, I_n^M, are calculated as $I_n^M = |A_n^M|^2$. The relative intensities of the diffraction peaks calculated from these models are compared with those determined from experimental synchrotron SAXS data. The electron densities of pure I-, S-, and O-domains used for these calculation are $\rho_e = 0.464$, 0.522, and 0.580 mol e^-/cm^3, respectively, based on reported densities at 140 °C.[67]

The experimental SAXS data were corrected by subtracting a background intensity using the approximation $I_{background}(q) = a + bq^2$, where a and b were adjustable parameters.[68] Figure 1b shows the SAXS profile for specimen ISO-21b as $I'q^2$ vs q incorporating the Lorentz correction ($I'q^2$) to the background-corrected intensity, I'. These were compared with all the candidate models. Figure 19 shows the relative intensities of SAXS peaks calculated from the three limiting models of segregation for specimen ISO-21b. Of the three cases shown,

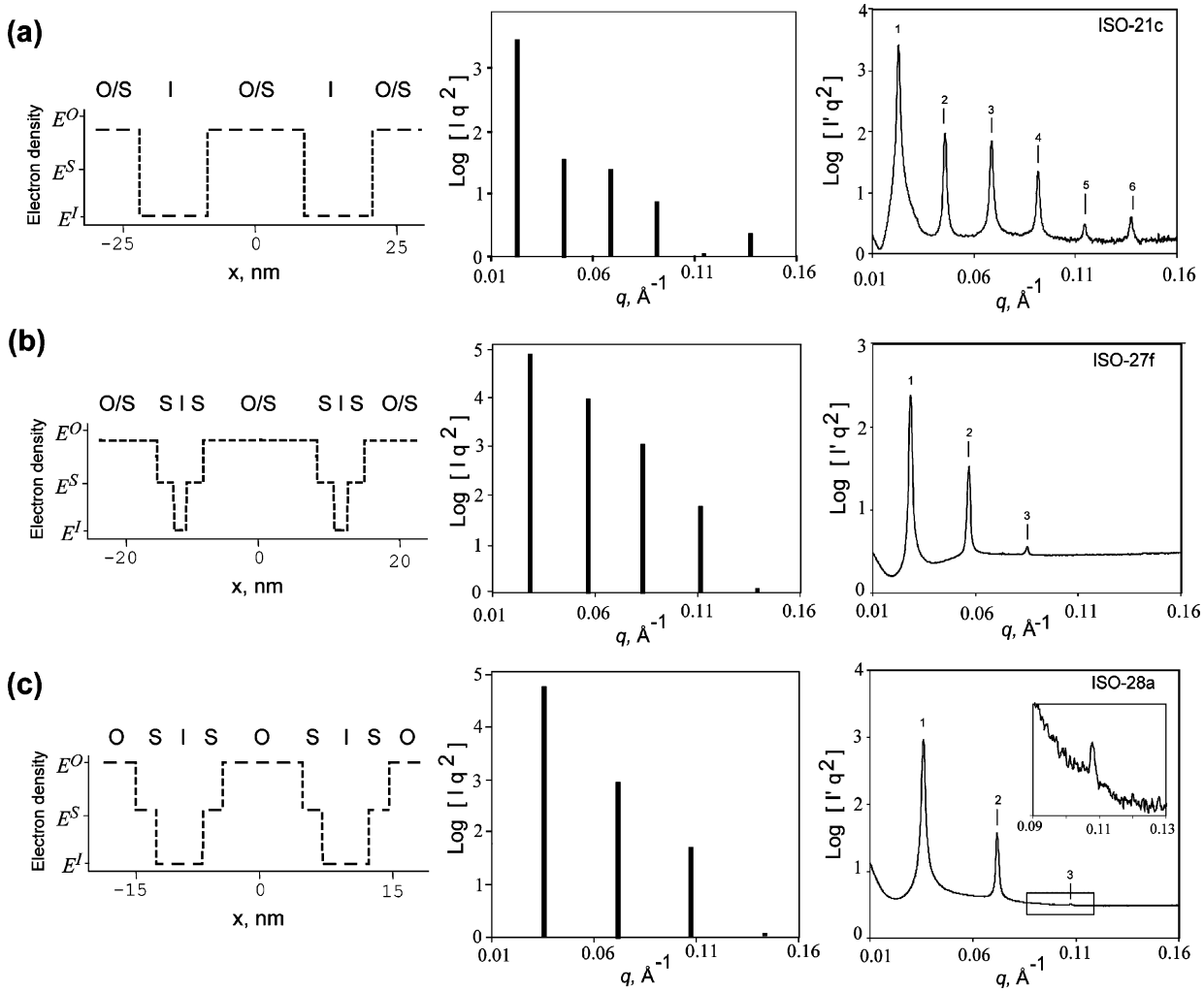

Figure 20. Best-fit models of lamellar segregation for (a) ISO-21c where S- and O-domains are completely mixed, (b) ISO-27f modeled by a state of partially mixed S (30%) and O, and (c) ISO-28a well segregated I-, S-, and O-domains. The experimental SAXS data were collected at 100 °C and Lorentz corrected after subtraction of background intensity.

the I-(S/O) model (Figure 19b) best represents the corrected SAXS data shown in Figure 1b; the relative intensities of all eight SAXS peaks follow the sequence for the two-state rectangular model. In contrast, the (I/S)-O model (Figure 19c) was eliminated since the $I(3q^*) > I(2q^*)$, while the I−S−O three-state model (Figure 19a) was disqualified since $I(5q^*) < I(6q^*)$, both inconsistent with experimental data. On the basis of this analysis, the state of segregation for ISO-21b was deduced to be S-domains significantly mixed with the O-domains. Here we note that the modeling effort could be further refined to account for the detailed relative peak intensities, which could provide additional Fourier coefficients and a more detailed composition profile. However, reductions in long-range order due to processing and sample deformation could result in an erroneous interpretation of the SAXS data.

Similar analysis of three more specimens located in the band of lamellae are shown in Figure 20. Specimen ISO-21c also was determined to contain mixed O and S blocks (Figure 20a), while the best fitting model for specimen ISO-27f corresponded to partial (30%) mixing of the S blocks with the O end blocks (Figure 20b). Specimen ISO-28a yielded a best model fit corresponding to three nearly completely segregated domains (see Figure 20c).

These results can be rationalized on the basis of specimen location in the phase map. ISO-28a is situated near the center of the lamellar band ($f_I = 0.28$, $f_S = 0.24$, and $f_O = 0.48$), with essentially balanced end-block dimensions and symmetric three-domain segregation. Specimen ISO-21c contains more I and less S, with about the same O content ($f_I = 0.44$, $f_S = 0.11$, and $f_O = 0.45$). Reducing the size of the S block makes it more miscible with O, consistent with the SAXS interpretation. Specimen ISO-21b responds in a similar fashion. At the other side of the band lies ISO-27f ($f_I = 0.08$, $f_S = 0.30$, and $f_O = 0.62$). Surprisingly, the model fit suggests three separate domains: partially mixed S with O, S, and I. We cannot explain why such a small I block would not combine with S, rather than S with O in this limit, particularly given the set of interaction parameters (eq 1). Perhaps this reflects a limitation of the technique, or the assumption that the binary interactions can be added together independently may be flawed.

In order to test the sensitivity of the calculated diffraction patterns to changes in model parameters, we analyzed the relative intensities of the computed scattering peaks as a function of the degree of partial mixing of S blocks with either O or I blocks. This analysis shows that the peak intensities respond substantially to modest changes in the degree of domain mixing; for example, the ratio of the third to first-order peak intensities increases by an order of magnitude when just 10% of S mixes with O in a triblock having a composition of I/S/O: 0.08/0.30/0.62. Representative calculations and a discussion are provided as Supporting Information. Although we believe these calculations are instructive, they cannot be interpreted as unique characterizations of the actual composition profiles. The modeling does depend on the assumptions of a boxlike composition profile with uniform domain compositions.

Conclusion

In this study we investigated the self-assembly of ISO melts, linear triblock copolymer, at weak to intermediate segregation strengths and across a wide composition range. Nearly monodisperse ISO triblocks were synthesized by a two-step living anionic polymerization technique, and the phases were characterized by a combination of experimental methods. In conjunction with our previous report, six different ordered state symmetries are identified: LAM, O^{70}, Q^{230}, Q^{214}, HEX, and BCC. O^{70} is stable in two distinct composition channels. Other intermediate states, tentatively assigned as HPL and mixed states of coexisting LAM and HEX, also were identified. The ISO system is "nonfrustrated" with the relative magnitudes of binary interaction parameters favoring two interfaces. The experimental phase map is asymmetric around the $f_I = f_O$ isopleth. This feature suggests that the composition dependence of the ordered phases depends sensitively on subtle variations in the segment−segment interaction parameters and possibly differences in the block statistical segment lengths, points worthy of further analyses. The effect of domain mixing was examined for several LAM phases by comparing experimental SAXS intensities with those calculated from simple rectangular models, demonstrating that mixing of domains can lead to the formation of two domain lamellae. The phase map provides a guide for further theoretical developments and a basis for developing a universal phase diagram for nonfrustrated ABC triblock copolymers.

Acknowledgment. This research was supported by the National Science Foundation (DMR-0220460). Use of the Advanced Photon Source was supported by the U.S. Department of Energy, Basic Energy Sciences, Office of Science, under Contract W-31-109-Eng-38. Experiments were conducted at research facilities of Dupont-Northwestern-Dow Collaborative Access Team, which is supported by DuPont, Dow, NSF (DMR-9304725), and the Illinois Department of Commerce and Grant IBHE HECA NWU 96. The authors are thankful for access to TEM and SAXS facilities at the Institute of Technology Characterization Facility at the University of Minnesota, which is partly supported by the NSF sponsored U of M MRSEC. The authors thank E. W. Cochran for using the SAXS analysis tool.

Supporting Information Available: Sensitivity analysis of calculated diffraction peak intensities. This material is available free of charge via the Internet at http://pubs.acs.org.

References and Notes

(1) Khandpur, A. K.; Foerster, S.; Bates, F. S.; Hamley, I. W.; Ryan, A. J.; Bras, W.; Almdal, K.; Mortensen, K. *Macromolecules* **1995**, *28*, 8796−8806.
(2) Bates, F. S.; Fredrickson, G. H. *Phys. Today* **1999**, *52*, 32−38.
(3) Leibler, L. *Macromolecules* **1980**, *13*, 1602−1617.
(4) Floudas, G.; Vazaiou, B.; Schipper, F.; Ulrich, R.; Wiesner, U.; Iatrou, H.; Hadjichristidis, N. *Macromolecules* **2001**, *34*, 2947−2957.
(5) Cochran, E. W.; Garcia-Cervera, C. J.; Fredrickson, G. H. *Macromolecules* **2006**, *39*, 2449−2451.
(6) Matsen, M. W.; Bates, F. S. *Macromolecules* **1996**, *29*, 1091−1098.
(7) Matsen, M. W.; Schick, M. *Macromolecules* **1994**, *27*, 4014−4015.
(8) Bailey, T. S.; Pham, H. D.; Bates, F. S. *Macromolecules* **2001**, *34*, 6994−7008.
(9) Breiner, U.; Krappe, U.; Jakob, T.; Abetz, V.; Stadler, R. *Polym. Bull. (Berlin)* **1998**, *40*, 219−226.
(10) Breiner, U.; Krappe, U.; Stadler, R. *Macromol. Rapid Commun.* **1996**, *17*, 567−575.
(11) Cochran, E. W.; Bates, F. S. *Phys. Rev. Lett.* **2004**, *93*, 087802.
(12) Epps, T. H.; Cochran, E. W.; Bailey, T. S.; Waletzko, R. S.; Hardy, C. M.; Bates, F. S. *Macromolecules* **2004**, *37*, 8325−8341.
(13) Shefelbine, T. A.; Vigild, M. E.; Matsen, M. W.; Hajduk, D. A.; Hillmyer, M. A.; Cussler, E. L.; Bates, F. S. *J. Am. Chem. Soc.* **1999**, *121*, 8457−8465.
(14) Stadler, R.; Auschra, C.; Beckman, J.; Krappe, U.; Voight-Martin, I.; Leibler, L. *Macromolecules* **1995**, *28*, 3080−3097.
(15) Matsushita, Y.; Suzuki, J.; Seki, M. *Physica B (Amsterdam)* **1998**, *248*, 238−242.
(16) Mogi, Y.; Nomura, M.; Kotsuji, H.; Ohnishi, K.; Matsushita, Y.; Noda, I. *Macromolecules* **1994**, *27*, 6755−6760.
(17) Mogi, Y.; Mori, K.; Matsushita, Y.; Noda, I. *Macromolecules* **1992**, *25*, 5412−5415.
(18) Seki, M.; Suzuki, J.; Matsushita, Y. *J. Appl. Crystallogr.* **2000**, *33*, 285−290.

(19) Suzuki, J.; Seki, M.; Matsushita, Y. *J. Chem. Phys.* **2000**, *112*, 4862−4868.
(20) Avgeropoulos, A.; Paraskeva, S.; Hadjichristidis, N.; Thomas, E. L. *Macromolecules* **2003**, *35*, 4030−4035.
(21) Mani, S.; Weiss, R. A.; Cantino, M. E.; Khairallah, L. H.; Hahn, S. F.; Williams, C. E. *Eur. Polym. J.* **1999**, *36*, 215−219.
(22) Ludwigs, S.; Boeker, A.; Voronov, A.; Rehse, N.; Magerle, R.; Krausch, G. *Nat. Mater.* **2003**, *2*.
(23) Beckmann, J.; Auschra, C.; Stadler, R. *Macromol. Rapid Commun.* **1994**, *15*, 67−72.
(24) Huckstadt, H.; Gopfert, A.; Abetz, V. *Polymer* **2000**, *41*, 9089−9094.
(25) Hueckstaedt, H.; Goldacker, T.; Goepfert, A.; Abetz, V. *Macromolecules* **2000**, *33*, 3757−3761.
(26) Abetz, V.; Goldacker, T. *Macromol. Rapid Commun.* **2000**, *21*, 16−34.
(27) Ott, H.; Abetz, V.; Altstadt, V. *Macromolecules* **2001**, *34*, 2121−2128.
(28) Bailey, T. S.; Hardy, C. M.; Epps, T. H.; Bates, F. S. *Macromolecules* **2002**, *35*, 7007−7017.
(29) Isono, Y.; Tanisugi, H.; Endo, K.; Fujimoto, T.; Hasegawa, H.; Hashimoto, T.; Kawai, H. *Macromolecules* **1983**, *16*, 5−10.
(30) Shibayama, M.; Hasegawa, H.; Hashimoto, T.; Kawai, H. *Macromolecules* **1982**, *15*, 274−280.
(31) Mogi, Y.; Mori, K.; Kotsuji, H.; Matsushita, Y.; Noda, I.; Han, C. C. *Macromolecules* **1993**, *26*, 5169−5173.
(32) Matsushita, Y.; Tamura, M.; Noda, I. *Macromolecules* **1994**, *27*, 3680−3682.
(33) Breiner, U.; Krappe, U.; Abetz, V.; Stadler, R. *Macromol. Chem. Phys.* **1997**, *198*, 1051−1083.
(34) Auschra, C.; Stadler, R. *Macromolecules* **1993**, *26*, 2171−2174.
(35) Brinkmann, S.; Stadler, R.; Thomas, E. L. *Macromolecules* **1998**, *31*, 6566−6572.
(36) Balsamo, V.; von Gyldenfeldt, F.; Stadler, R. *Macromolecules* **1999**, *32*, 1226−1232.
(37) Epps, T. H.; Bates, F. S. *Macromolecules* **2006**, *39*, 2676−2682.
(38) Epps, T. H.; Chatterjee, J.; Bates, F. S. *Macromolecules* **2005**, *38*, 8775−8784.
(39) Hillmyer, M. A.; Bates, F. S. *Macromolecules* **1996**, *29*, 6994−7002.
(40) Fetters, L. J.; Lohse, D. J.; Richter, D.; Witten, T. A.; Zirkel, A. *Macromolecules* **1994**, *27*, 4639−4647.
(41) Balsara, N. P.; Perahia, D.; Safinya, C. R.; Tirrell, M.; Lodge, T. P. *Macromolecues* **1992**, *25*, 3896−3901.
(42) Balsara, N. P.; Garetz, B. A.; Dai, H. J. *Macromolecules* **1992**, *25*, 6072−6074.
(43) Hanley, K. J.; Lodge, T. P.; Huang, C.-I. *Macromolecules* **2000**, *33*, 5918−5931.
(44) Koppi, K. A.; Tirrell, M.; Bates, F. S.; Almdal, K.; Mortensen, K. *J. Rheol.* **1994**, *38*, 999−1027.
(45) Kossuth, M. B.; Morse, D. C.; Bates, F. S. *J. Rheol.* **1999**, *43*, 167−196.
(46) Theo, H., Ed. *International Tables for Crystallography*, 4th ed.; Kluwer Academic Publishers: Dordrecht, 1995; Vol. A (space-group symmetry).
(47) Hajduk, D. A.; Harper, P. E.; Gruner, S. M.; Honeker, C. C.; Kim, G.; Thomas, E. L.; Fetters, L. J. *Macromolecules* **1994**, *27*, 4063−4075.
(48) Hillmyer, M. A.; Bates, F. S.; Almdal, K.; Mortensen, K.; Ryan, A. J.; Fairclough, J. P. A. *Science* **1996**, *271*, 976−978.
(49) Zhao, J.; Majumdar, B.; Schulz, M. F.; Bates, F. S.; Almdal, K.; Mortensen, K.; Hajduk, D. A.; Gruner, S. M. *Macromolecules* **1996**, *29*, 1204−1215.
(50) Zhu, L.; Huang, P. D. C. S. Z.; Ge, Q.; Quirk, R. P.; Thomas, E. L.; Lotz, B.; Wittmann, J.-C.; Benjamin, H.; Yeh, F.; Liu, L. *Phys. Rev. Lett.* **2001**, *86*, 6030−6033.
(51) Loo, Y.-L.; Register, R. A.; Adamson, D. H.; Ryan, A. J. *Macromolecules* **2005**, *38*, 4947−4949.
(52) Imai, M.; Sakai, K.; Kikuchi, M.; Nakaya, K.; Saeki, A.; Teramoto, T. *J. Chem. Phys.* **2005**, *122*, 214906/214901−214906/214910.
(53) Hajduk, D. A.; Ho, R.-M.; Hillmyer, M. A.; Bates, F. S.; Almdal, K. *J. Phys. Chem. B* **1998**, *102*, 1356−1363.
(54) Hajduk, D. A.; Takenouchi, H.; Hillmyer, M. A.; Bates, F. S.; Vigild, M. E.; Almdal, K. *Macromolecules* **1997**, *30*, 3788−3795.
(55) Vigild, M. E.; Almdal, K.; Mortensen, K.; Hamley, I. W.; Fairclough, J. P. A.; Ryan, A. J. *Macromolecules* **1998**, *31*, 5702−5716.
(56) Ahn, J.-H.; Zin, W.-C. *Macromolecules* **2000**, *33*, 641−644.
(57) Lipic, P. M.; Bates, F. S.; Matsen, M. W. *J. Polym. Sci., Part B: Polym. Phys.* **1999**, *37*, 2229−2238.
(58) Tyler, C. A.; Morse, D. C. *Phys. Rev. Lett.* **2005**, *94*, 208302.
(59) Frielinghaus, H.; Hermsdorf, N.; Almdal, K.; Mortensen, K. M. L.; Corvazier, L.; Fairclough, J. P. A.; Ryan, A. J. O. P. D.; Hamley, I. W. *Europhys. Lett.* **2001**, *53*, 680−686.
(60) Bailey, T. S. Ph.D. Thesis, University of Minnesota, 2001.
(61) Tyler, C. A. Ph.D. Thesis, University of Minnesota, 2004.
(62) Shefelbine, T. A.; Vigild, M. E.; Matsen, M. W.; Hajduk, D. A.; Hillmyer, M. A.; Cussler, E. L.; Bates, F. S. *J. Am. Chem. Soc.* **1999**, *121*, 8457−8465.
(63) Sugiyama, M.; Shefelbine, T. A.; Vigild, M. E.; Bates, F. S. *J. Phys. Chem. B* **2001**, *105*, 12448−12460.
(64) Matsen, M. W.; Bates, F. S. *J. Chem. Phys.* **1997**, *106*, 2436−2448.
(65) Zeng, X.; Ungar, G. *Polymer* **1998**, *39*, 4523−4533.
(66) Zeng, X. B.; Ungar, G. *Phys. Rev. Lett.* **2001**, *86*, 48754878.
(67) Cochran, E. W.; Morse, D. C.; Bates, F. S. *Macromolecules* **2003**, *36*, 782−792.
(68) Wolff, T.; Burger, C.; Ruland, W. *Macromolecules* **1994**, *27*, 3301−3309.

MA062249S